

ATOMS: ALMA Three-millimeter Observations of Massive Star-forming regions – VI. On the formation of the "L" type filament in G286.21+0.17

Jian-Wen Zhou,^{*1,2} Tie Liu,^{†3,4} Jin-Zeng Li,^{‡1} Hong-Li Liu,^{5,6} Ke Wang,⁷ Feng-Wei Xu,⁸ Kee Chang Won Lee,^{9,10} Lokesh Dewangan,¹¹ Ken'ichi Tatematsu,¹² Shanghuo Li,⁹ Xun-Chuan Liu Mengyao Tang,¹⁴ Zhiyuan Ren,¹ Guo-Yin Zhang,¹ Chao Zhang,⁵ Rong Liu,^{1,2} Qiu-Yi Luo,^{3,2} Isabelle Ristorcelli¹³

Affiliations are listed at the end of the paper

Accepted XXX. Received YYY; in original form ZZZ

ABSTRACT

Filaments play an important role in star formation, but the formation process of filaments themselves is still unclear. The high-mass star forming clump G286.21+0.17 (G286 for short) that contains an "L" type filament was thought to undergo global collapse. Our high resolution ALMA band 3 observations resolve the gas kinematics of G286 and reveal two sub-clumps with very different velocities inside it. We find that the "blue profile" (an indicator of gas infall) of HCO⁺ lines in single dish observations of G286 is actually caused by gas emission from the two sub-clumps rather than gas infall. We advise great caution in interpreting gas kinematics (e.g., infall) from line profiles toward distant massive clumps in single dish observations. Energetic outflows are identified in G286 but the outflows are not strong enough to drive expansion of the two sub-clumps. The two parts of the "L" type filament ("NW-SE" and "NE-SW" filaments) show prominent velocity gradients perpendicular to their major axes, indicating that they are likely formed due to large-scale compression flows. We argue that the large-scale compression flows could be induced by the expansion of nearby giant HII regions. The "NW-SE" and "NE-SW" filaments seem to be in collision, and a large amount of gas has been accumulated in the junction region where the most massive core G286c1 forms.

Key words: stars: formation; stars: protostars; ISM: kinematics and dynamics; ISM: HII regions; ISM: clouds

1 INTRODUCTION

High-mass stars that generally form in clusters are born in dense molecular clumps. However, the conversion of turbulent, self-gravitating, dense molecular gas clumps into high-mass stars as well as star clusters remains an open question in astrophysics (Zinnecker & Yorke 2007; Motte et al. 2018; Jackson et al. 2019). At present, there are several theoretical models for high-mass star formation. The "competitive accretion" model (Bonnell et al. 1997, 2001) explicitly relies on the funneling of gas into the center of the clump in order to provide fresh material for the central cores to accumulate enough mass to build up a high-mass star. In other words, this model predicts that the clump must be undergoing global collapse. The "global hierarchical collapse"

model (Vázquez-Semadeni et al. 2009, 2017) is an extension of the competitive accretion model when accretion through inflowing gas streams driven by gravity replaces the Bondi–Hoyle accretion (Smith et al. 2009). In this scenario, high-mass protostars would then be fed from the gas of their surrounding massive dense cores (MDCs)/clumps (Motte et al. 2018). Although the "turbulent core accretion" model (McKee & Tan 2003; Krumholz et al. 2005) has no such explicit requirement, the formation of the parsec-scale dense clump itself almost certainly results from the gravitational collapse of a larger giant molecular cloud. Thus, for all of these theoretical models, large-scale (parsec-scale) infall motions due to gravitational collapse are expected (Jackson et al. 2019). Therefore, observations of gas infall motion in protoclusters are essential to test these models. Global collapse of protoclusters or massive clumps has been suggested in some previous observations (e.g., Barnes et al. 2010; Liu et al. 2013; Peretto et al. 2013; He et al. 2015; Yuan et al. 2017).

The existence of filaments in the interstellar medium has

* E-mail: zjw@nao.cas.cn

† E-mail: liutie@shao.ac.cn

‡ E-mail: ljz@nao.cas.cn

been known for a long time. In particular, the imaging surveys with the Herschel observatory have greatly promoted the studies of filamentary structures in molecular clouds (André et al. 2010; Molinari et al. 2010; Arzoumanian et al. 2011, 2019). Majority of the prestellar cores or protostars are found to be embedded within such filamentary structures, indicating that dense molecular filaments are the important sites of star formation (Marsh et al. 2016; Könyves et al. 2015, 2020). Filaments will fragment into dense cores when the filaments reach a critical density or line-mass (Vazquez-Semadeni 1994; Krumholz et al. 2007; Zhang et al. 2020). Magnetic fields also play an important role in stabilizing filaments (Fiege & Pudritz 2000; Hennebelle & André 2013; Gómez et al. 2018). Although the role of filaments in star formation is increasingly confirmed by observations, the formation process of filaments themselves is still unclear (André et al. 2014).

G286.21+0.17 (hereafter G286) is a massive protocluster site associated with the η Car giant molecular cloud at a distance of 2.5 ± 0.3 kpc, in the Carina spiral arm (e.g., Barnes et al. 2010, hereafter B10; Andersen et al. 2017). Through observations of molecular lines, B10 determined several parameters about G286 region: the size ~ 0.9 pc, the luminosity $\sim (2-3) \times 10^4 L_{\odot}$, and the mass $\sim 20000 M_{\odot}$. From the line profiles of the J=1-0 and J=4-3 transitions of HCO⁺ and H¹³CO⁺ line emission, B10 argued that G286 is undergoing global collapse and they found one of the largest such infall rates yet measured in protoclusters, $\sim 3 \times 10^{-2} M_{\odot} \text{ yr}^{-1}$. From *Herschel* column density map, Ohlendorf et al. (2013) determined the mass of the cloud is $\sim 2105 M_{\odot}$ by integrating over a $2.23 \text{ pc} \times 2.23 \text{ pc}$ box around the clump. The densest part of G286 region, or the dense clump associated with the infrared source IRAS 10365–5803, has a mass of only $\sim 470 M_{\odot}$ (Faúndez et al. 2004). This work is focused on the dense clump.

Andersen et al. (2017) suggests the cluster are very young with a rich population of pre-main-sequence stars with a disk fraction ranging from 27% to 44% for a magnitude and extinction limited sample. Cheng et al. (2020b) presents a near-infrared (NIR) variability analysis toward the G286 protocluster, suggesting it as being an extreme case of an outburst event that is still ongoing. These properties make G286 a particularly interesting site of high-star formation. Cheng et al. (2018) present the 1.3 mm ALMA continuum observation of G286 and an analysis of the core mass function (CMF) in this region. Subsequently, Cheng et al. (2020a) (hereafter C20) present a follow-up study of multiple spectral lines from the same ALMA observations to investigate the gas kinematics and dynamics of G286 from clump to core scales. In this paper, we use new ALMA data from the ATOMS survey (see Sec. 2.2) to revisit the G286 clump, focusing on testing the global infall proposed by B10. We also discuss the outflows, filaments and star formation history in this region.

2 OBSERVATIONS

2.1 Single dish data

The single-pointing observations with the Atacama Pathfinder Experiment (Güsten et al. 2006, APEX) in CO (4-3) and C¹⁷O (3-2) lines were conducted from August 8th to 10th, 2015. All observations were performed using the position switching mode, the pointing position is RA=10:38:32.00, Dec=-58:19:15.20. The reference position was carefully selected in a circular region with a diameter of 3 arcdeg centered at the “on” source position, which has no or extremely weak CO emission based on previous CO surveys of the

Milky Way (Dame et al. 2001). The antenna system temperatures range from 236 to 255 K, and from 865 to 1145 K respectively, during C¹⁷O (3-2) and CO (4-3) observations. The frontend used was the MPIFR dual channel FLASH receiver (460 and 810 GHz) and APEX2 receiver (345 GHz) (Heyminck et al. 2006), along with the APEX digital Fast Fourier Transform Spectrometer backends (Klein et al. 2006, FFTS). The lines were covered with 2048 channels within a bandwidth of 1 GHz. We have smoothed the spectra to 0.27 and 0.4 km s⁻¹ resolution for CO (4-3) and C¹⁷O (3-2) lines. The mean rms noise levels are 0.19 and 0.14 K for CO (4-3) and C¹⁷O (3-2) lines, respectively. The beam sizes are 13'' and 18'' for CO (4-3) and C¹⁷O (3-2) lines, respectively. More details of the APEX observations were summarised in Yue et al. (2021).

The single pointing observations of G286 with the Atacama Submillimeter Telescope Experiment (ASTE) 10 m telescope were conducted between 2014 July 1st and 4th (Liu et al. 2016b). All observations were performed using the position switching mode, the pointing position is RA=10:38:32.02, Dec=-58:19:15.10. The two-side band single-polarization heterodyne receiver DASH345/CATS345, operating at frequencies of 324–372 GHz was used to observe HCN (4-3) and CS (7-6) lines simultaneously. We used the MAC spectrometer with a spectral resolution of 0.5 MHz or 0.42 km s⁻¹. The beam size at 354 GHz is $\sim 22''$. The main beam efficiency was ~ 0.6 . The system temperature varied from 400 to 500 K during observations. The rms level per channel is ~ 0.1 -0.2 K in antenna temperature. More details of the ASTE observations were summarised in Liu et al. (2016b).

2.2 ALMA observations

We use ALMA data from the ATOMS survey (Project ID: 2019.1.00685.S; PI: Tie Liu). The ACA 7m observations of G286 (or I10365-5803) were conducted on the 19th October, 2019. The 12-m array observations of G286 were conducted on the 2nd November, 2019. The typical 12-m array time on source is ~ 3 minutes, while typical ACA 7m observing time per source is ~ 8 minutes. The angular resolution and maximum recovered angular scale for the ACA 7m observations are $\sim 13''$ and $\sim 73''$, respectively. The angular resolution and maximum recovering angular scale for the 12-m array observations are $\sim 1.7''$ and $\sim 19''$, respectively. The achieved angular resolutions of the 12-m array observations for molecular lines are usually better than 2'' (or ~ 0.024 pc at 2.5 kpc distance), enabling us to resolve dense cores (~ 0.1 pc in size) in G286. More details of the ALMA observations were summarised in Liu et al. (2020a,b).

Calibration and imaging were carried out using the CASA software package version 5.6 (McMullin et al. 2007). The ACA 7m data and ALMA 12m array data were calibrated separately. Then the visibility data from the ACA 7m and ALMA 12m array configurations were combined and later imaged in CASA. For each source, each spectral window (spw), a line-free frequency range is automatically determined using the ALMA pipeline (see ALMA technical handbook). This frequency range is used to (a) subtract continuum from line emission in the visibility domain, and (b) make continuum images. Continuum images are made from multi-frequency synthesis of data in this line-free frequency ranges in the two 1.875 GHz wide spectral windows, spw 7 and 8, centered on ~ 99.4 GHz (or 3 mm). Visibility data from the ALMA 12m and ACA 7m arrays is jointly cleaned using task tclean in CASA 5.6. We used natural weighting and a multiscale deconvolver, for an optimized sensitivity and image quality. All images are primary-beam corrected. The continuum image reaches a 1σ rms noise of 0.21 mJy in a synthe-

Table 1. Main targeted molecular lines in ALMA 7m+12m combined data

| Molecule | rms levels (Jy beam ⁻¹) | spectral resolution (km s ⁻¹) | beam sizes |
|---------------------------------------|--|--|-----------------|
| HCO ⁺ (1-0) | 0.012 | 0.103 | 2.36'' × 2.53'' |
| H ¹³ CO ⁺ (1-0) | 0.008 | 0.211 | 2.40'' × 2.61'' |
| HC ₃ N (11-10) | 0.004 | 1.463 | 2.09'' × 2.26'' |
| SiO (2-1) | 0.008 | 0.211 | 2.39'' × 2.63'' |
| SO (3(2)-2(1)) | 0.004 | 1.474 | 2.14'' × 2.33'' |
| CCH (1-0) | 0.008 | 0.210 | 2.39'' × 2.60'' |
| CS (2-1) | 0.004 | 1.494 | 2.14'' × 2.33'' |

sized beam of $2.12'' \times 2.29''$ (PA = -56.74°). For molecular lines, we focus on HCO⁺ (1-0), H¹³CO⁺ (1-0), HC₃N (11-10), SiO (2-1), SO (3(2)-2(1)), CCH (1-0) and CS (2-1), which are summarized in Table 1 for the 7m+12m combined data.

2.3 Archived continuum emission data

To study the physical characteristics of G286 clump and the interaction between the clump and its surrounding environment, auxiliary data of images were complemented by the GLIMPSE (Benjamin et al. 2003), MIPS GAL (Carey et al. 2009) and Herschel Infrared GALactic plane survey (Molinari et al. 2010, 2016). The images of the Spitzer Infrared Array Camera (IRAC) at 3.6, 4.5, 5.8, and 8.0 μm , together with the Multiband Imaging Photometer for Spitzer (MIPS) at 24 μm were retrieved from the Spitzer Archive. The angular resolutions of the images in the IRAC bands are $< 2''$ and it is $\sim 6''.0$ in the MIPS 24 μm band. The data of Herschel Archive were obtained with the Photodetector Array Camera and Spectrometer (PACS, 70 and 160 μm) (Poglitsch et al. 2010), the measured angular resolutions of the data at these bands are $10''.7$ and $13''.9$ (Traficante et al. 2011). All of the Hi-GAL data have been processed by PPMAP procedure, by which high resolution column density and dust temperature maps could be obtained. The resolution of column density and dust temperature maps is $\sim 12''$, and the resulting data is available online¹ (Marsh et al. 2017). We also used ATLASGAL+Planck 870 μm data (ATLASGAL combined with Planck data), which are sensitive to a wide range of spatial scales at a resolution of $\sim 21''$ (Csengeri et al. 2016a).

3 RESULTS

3.1 Continuum emission

Fig. 1(a) presents a large-scale composite color map of the natal molecular cloud of G286 clump. Fig. 1(b) is the blow-up image of G286 clump. The red circles in both panels (a) and (b) show the FOV of the ALMA 12-m array observations. Our ALMA observations cover the central region of the G286 clump. Fig. 2 shows the column density and dust temperature maps of G286 clump derived with the PPMAP procedure. The average dust temperature over the central region of G286 clump (i.e. inside the red circle with a radius of $R \sim 0.44$ pc, which is roughly the FWHM radius of the ALMA 12m-array FOV) is ~ 21.4 K. The average column density N within

the circle is about $5.66 \times 10^{22} \text{ cm}^{-2}$. Assuming the spherical geometry of clump, the number density is $n = N/2R$, then the mass of the central region in G286 clump is:

$$M = \frac{4}{3} \pi R^3 \mu m_{\text{H}} n \quad (1)$$

,where $\mu = 2.37$ is the mean molecular weight per "free particle" (H₂ and He, the number of metal particles is negligible), m_{H} and n are atomic hydrogen mass and molecular hydrogen number density. We obtain $M \sim 1021 M_{\odot}$.

A clear temperature gradient appears in the northwest-southeast direction of the clump in Fig. 2(b), indicating that the G286 clump is externally heated by the HII region A. The HII region A is visible as a Br- γ emission nebula and is exactly coincident with a centimetre-continuum point source (see B10 for details). Protostars have formed inside the G286 clump, which are clearly seen as point sources in Spitzer images. Based on the previous studies, G286 clump is on the edge of HII region A (see B10). Both G286 and HII region A are found to be near HII region B (Gum31), which is at the same distance ($d \sim 2.5$ kpc) and is excited by a young stellar cluster NGC3324 (Cappa et al. 2008; Barnes et al. 2010; Ohlendorf et al. 2013; Andersen et al. 2017). HII region B is strongly interacting with the surrounding interstellar medium, and it may likely also affect the evolution of G286 and HII region A. In Sec. 4.3, we will discuss in detail the effect of HII region A and B on star formation history in the G286 clump.

As shown in the Fig. 1(b), the main structure of the G286 clump in ALMA 3 mm continuum emission appears as "L" shape, which is labeled as "NE-SW" and "NW-SE" filaments in Fig. 1 of C20. Fig. 3 shows the 3 mm continuum emission. The blue contours show compact cores extracted from the 3 mm continuum emission with the Dendrogram algorithm², and the cores are generally distributed along the "L" structure. Red lines show the skeletons of sub-filaments identified with the FILFINDER algorithm (Koch & Rosolowsky 2015). The length of longest sub-filament is ~ 0.77 pc. The most massive cores, which are marked by bold "+" in Fig. 3, are found to be located along the longest filament. We fit the radial profiles of longest sub-filament with the Radfil algorithm (Zucker & Chen 2018) and obtain the width (deconvolved FWHM) of longest filament, $W \sim 0.075$ pc (the detailed description of the procedures is given in Appendix. A).

The 76 dense cores identified by 1.3mm continuum in C20 are marked by "+" in Fig. 3. The 1.3mm continuum emission which has higher sensitivity reveals more fainter cores than the 3mm continuum emission. Fig. 4 shows a dendrogram tree obtained from the nearest neighbor separation (NNS) analysis to 76 dense cores (with the scipy function cluster.hierarchy.linkage and the "ward" method). The dense cores can be broadly divided into three clusters (A, B, C). Dense cores in cluster C (blue dots) are located beyond the FOV of our ALMA observations, and thus they are excluded in this study. The remaining clusters are named as sub-clump A and sub-clump B. In C20, they divided the cores into two groups "blue" and "red" based on their velocity differences. Interestingly, we find that sub-clumps A and B identified in the NNS analysis match the "red" group and "blue" groups by C20 well, respectively, suggesting that they are physically separated. We roughly mark the locations of two sub-clumps in Fig. 3 with blue and red dashed circles.

¹ <http://www.astro.cardiff.ac.uk/research/ViaLactea/>

² <https://dendrograms.readthedocs.io/en/stable/>

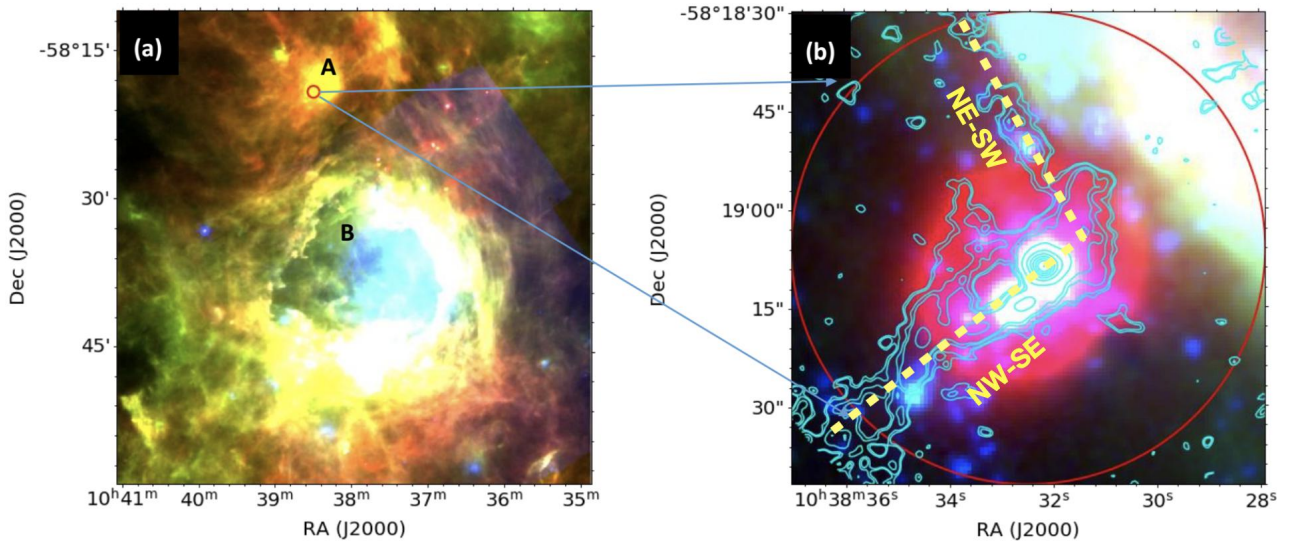


Figure 1. (a) Three-color image of G286 and its surrounding environment constructed by combining Herschel PACS 160 (red), 70 (green) μm and Spitzer 24 μm (blue). Central coordinates of this figure is (Ra, Dec)=(159.50°, -58.58°). Area of this region is $0.8^\circ \times 0.8^\circ$. Red circle is the FOV of the ALMA 12m array observations; (b) Three-color image of the region inside red circle constructed by combining Spitzer IRAC 4.5 (blue), 5.8 (green) μm and Herschel PACS 70 μm (red). Cyan contours show the 3 mm continuum image combined ALMA 12 and 7 m array data. Contour levels are $1\sigma \times (1.5, 2, 4, 8, 16, 32, 64)$ with $\sigma = 0.21$ mJy/beam. The two filaments "NE-SW" and "NW-SE" are marked with yellow dashed lines.

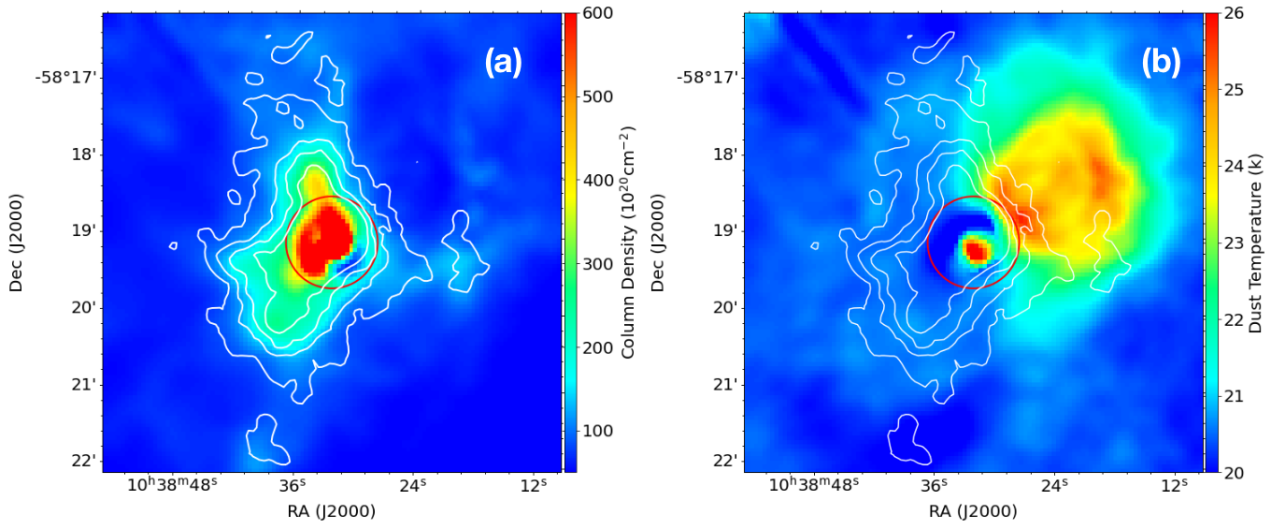


Figure 2. Column density map and temperature distribution map derived with the PPMAP procedure, the size of region is $6' \times 6'$, red circle is the FOV of the ALMA 12m array observations, white contour is the data of ATLASGAL+Planck 870 μm . Contour levels are $1\sigma \times (3, 4.5, 6, 8)$ with $\sigma = 0.20$ Jy/beam.

3.2 Molecular line emission from single dish and ACA 7m observation

In B10, they found that the $J=1-0$ and $J=4-3$ of lines HCO^+ show double peak profiles with the blueshifted peak stronger than the redshifted one. Such "blue profile" was argued as evidence of large-scale gravitational infall in the dense gas. Fig. 5(a) shows the observation with ASTE in G286 region, the double-peak profile of HCN (4-3) is barely seen, but the line profile of CS (7-6) looks like a single-peak. This is due to the poor spectral resolution ($\sim 0.8 \text{ km s}^{-1}$) in ASTE observations. The line profiles in ASTE observations are not well resolved. Moreover, we also observed G286 region with the APEX telescope (Fig. 5(b)). The optically thick CO $J=4-3$ line shows a red profile rather than a blue profile, it also shows

high velocity wing emission, suggesting the existence of energetic outflows in the G286 clump. The optically thin C^{17}O $J=3-2$ line is single peaked but skewed to the redshifted side.

The difference of the line profiles in ASTE and APEX observations could be related to the following two aspects: (1) Due to the poor spatial resolutions, single dish observations usually can not resolve the gas kinematics within massive clumps. Various line profiles could be caused by a mixture of gas kinematics (outflows, infall, rotation et al.) within a large beam. (2) Molecular lines with different critical densities or excitation conditions may trace various layers of the clump, resulting in different line profiles.

Therefore, we advise great caution in interpreting gas kinematics (e.g., infall) from line profiles toward distant massive clumps in single dish observations. Fig. 5(c) presents the spectra of

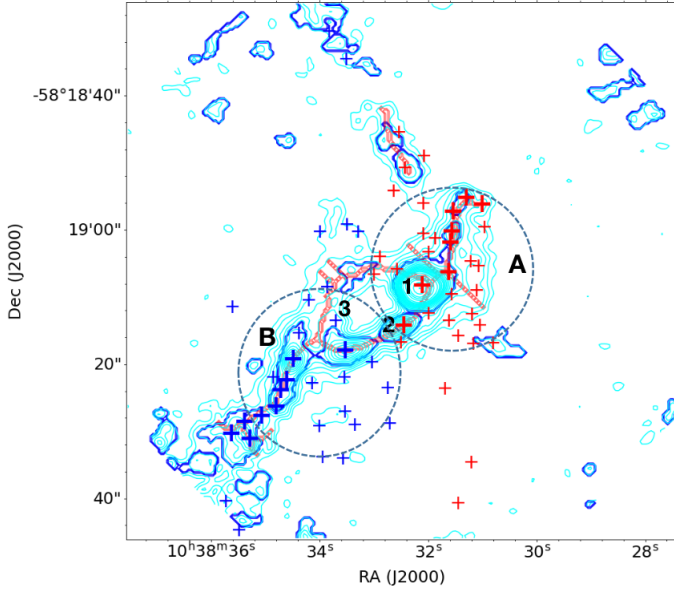


Figure 3. 3 mm continuum emission from 12m+7m data is shown as cyan contours with contour levels $1\sigma \times (1.5, 2, 2.8, 3.6, 4.4$ to 12 by 0.4 steps, 12 to 15.2 by 0.8 steps, 18, 24, 30, 36, 48, 60) with $\sigma=0.21$ mJy/beam, and blue contours are the clumps found by Dendrogram algorithm. Red line is the skeleton of filament recognized by FILFINDER algorithm from 3 mm continuum emission. "+" represents dense cores identified by C20, and bold "+" indicates the cores on the longest filament. Blue dashed circles mark two sub-clumps A and B identified in Fig. 4. Red "+" show cores of sub-clump A, blue "+" for sub-clump B. The black number represents the serial number of the core corresponding to "+" (G286c1, G286c2 and G286c3).

HCO^+ J=1-0 and H^{13}CO^+ J=1-0 from ACA 7m observations. The FOV of ACA 7m array is about two times larger than the ALMA 12-m array, and thus ACA 7m array data are useful to study gas kinematics at a larger scale. The spectra were averaged over a region with a size of $36''$, which is comparable to the Mopra beam size in B10. Both HCO^+ J=1-0 and H^{13}CO^+ J=1-0 show double peak profiles. The HCO^+ J=1-0 line profile in ACA 7m observations is blue profile, similar to the line profile in Mopra observations of B10. In B10, they argued that the optically thin line H^{13}CO^+ is single peaked. However, in ACA 7m observations, the H^{13}CO^+ J=1-0 line is double-peak profile. The moment maps of molecular line emission in ACA 7m array data are shown in Appendix. B.

3.3 Molecular line emission from combined ALMA 12-m array and ACA data

To further study the gas kinematics in the G286 clump, we use the ALMA 12m+7m combined data for HCO^+ (1-0), H^{13}CO^+ (1-0), CCH (1-0), CS (2-1) and HC_3N (11-10). Fig. 6 shows the grid map of H^{13}CO^+ (1-0). From left to right of the map, the emission peaks of H^{13}CO^+ (1-0) change from redshift to blueshift with respect to the systemic velocity. The averaged spectra and grid maps of other lines are shown in Appendix. B, which having similar patterns to that of H^{13}CO^+ (1-0).

Figure 7 presents the moment maps of HCO^+ (1-0), H^{13}CO^+ (1-0), CCH (1-0), and CS (2-1) in 7m+12m data. Two spatially separated sub-clumps are clearly seen from these moment maps. To reduce outflow contamination, we make moment 1 maps in the narrow velocity range of -23 km s^{-1} to -16.5 km s^{-1} . The mo-

Table 2. Fitting parameters of SiO lines toward G286.21+0.17. Peak intensity I_p , velocity V_p corresponding to I_p and line width FWHM. r is the radius of black circle representing the area over which the averaged spectra are taken at each position marked in Fig. 9.

| Position | r (arcsecond) | I_p (Jy beam $^{-1}$) | FWHM (km s $^{-1}$) | V_p (km s $^{-1}$) |
|----------|--------------------|-----------------------------|-------------------------|--------------------------|
| A | 2.30 | 0.032 | 3.74 | -21.73 |
| | | 0.018 | 8.01 | -25.21 |
| B | 6.06 | 0.021 | 8.11 | -25.75 |
| | | 0.007 | 19.69 | -36.44 |
| C | 2.10 | 0.028 | 3.43 | -20.76 |
| | | 0.005 | 20.25 | -15.32 |
| D | 2.10 | 0.031 | 2.65 | -18.71 |
| E | 2.76 | 0.033 | 6.04 | -20.82 |
| | | 0.017 | 9.06 | -17.35 |
| F | 2.76 | 0.027 | 5.49 | -22.82 |
| | | 0.019 | 10.23 | -18.67 |

ment 1 maps shown in the last row of Figure 7 also clearly reveal the large-scale velocity gradients along the north-west to south-east direction and the boundary of the two sub-clumps. These high resolution moment maps again confirm that the double peak profiles of molecular lines in single dish observations indeed come from the mixture of gas emission in two sub-clumps.

HC_3N (11-10) is a good tracer of dense molecular gas (Liu et al. 2020a). As shown in Fig. 8a, the morphology of HC_3N (11-10) emission matches with the 3 mm continuum emission very well. In addition, the clumps and/or cores found by dendrogram algorithm in 3mm continuum and in the moment 0 map of HC_3N match very well (see Fig. 8b). Hence, we suggest HC_3N can be a good tracer of filaments and dense cores. The two brightest cores (marked as "1" and "2" in Fig. 8a or Fig. 3) are associated with two young stellar objects, which are clearly seen in Spitzer IRAC bands (Fig. 1). Since the intensity sensitivity of HC_3N is higher than 3 mm continuum, the former reveals more structures than the latter. The "+" show the dense cores identified by C20 in 1.3 mm continuum. It can be seen that the dense cores traced by 1.3 mm emission do not always coincide well with HC_3N gas cores, which could be caused either by some chemical effect or different sensitivity between line and continuum data. In the northern part of G286, the HC_3N emission is embraced by the Spitzer $8 \mu\text{m}$ emission, which traces the PDR of the HII region to the north-west. It indicates that the HII region may greatly affect the dense gas distribution in the northern part of G286. Moreover, there is a cavity in the middle part of the moment 0 map of HC_3N , which is like the cavity blown out by outflows (see Sec. 3.4).

3.4 Molecular Outflows and shocked gas

As shown in Fig. 5(c) and Fig. B2, the spectral lines of optically thick HCO^+ (1-0) and CS (2-1) have obvious high-velocity line wings, strongly suggesting the existence of energetic outflows. Considering that most of the optically thin H^{13}CO^+ (1-0) line emission is between -23 km s^{-1} and -16.5 km s^{-1} , the velocity intervals for redshifted and blueshifted high velocity emission of HCO^+ (1-0) and CS (2-1) lines are defined as $[-16.5, 5] \text{ km s}^{-1}$ and $[-41, -23] \text{ km s}^{-1}$, respectively. The integrated intensity maps of outflow emission (or outflow lobes) are shown in Fig. 9. The outflow seems to be driven by G286c1 (marked as "1" in Fig. 8a or Fig. 3). The outflow is well aligned with the skeleton of the

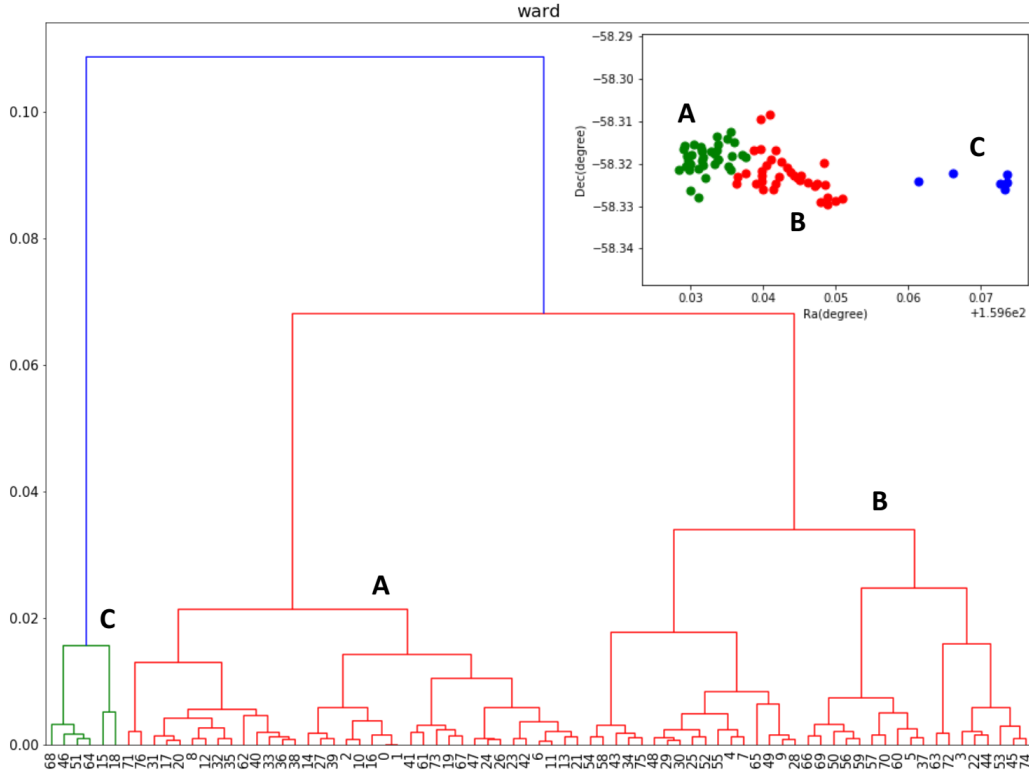


Figure 4. Three clusters of 76 dense cores in G286 clump by applying a nearest neighbor separation (NNS) analysis.

longest sub-filament. In addition, the cavities in the moment 0 map of HC_3N (11-10) and also in the 3mm emission continuum (see Fig. 8a) are approximately along the blueshifted outflow lobe. Naturally, we can infer that the outflows swept gas out, and the mechanical force of outflows could contribute to the formation of the cavity.

As shown in Fig. 9a, SiO (2-1) emission reveals several bright knots along the outflows, which are marked from "A" to "F". Knots A and B are located within the blueshifted lobe of outflow and others (Knots C, D, E, F) within the redshifted lobe. Almost every SiO emission knot has a corresponding dense core. Fig. 10 present averaged SiO spectra over the area defined by black circle in Fig. 9a. The spectra can be well fitted with double gaussian profiles (a narrow component plus a broad component). The Gaussian fitting results are summarized in Tab. 2. The line widths of broad components in SiO emission are much larger than 8 km s^{-1} , also suggesting they are affected by outflow shocks.

Besides the broad components, SiO lines also show a narrow component. Narrow SiO (2-1) emission has been detected in infrared dark clouds (Jiménez-Serra et al. 2010; Csengeri et al. 2016b; Cosentino et al. 2018, 2020) and high-mass proto-cluster forming regions (Nguyen-Lu'o'ng et al. 2013; Louvet et al. 2016; Csengeri et al. 2016b; Liu et al. 2020a). Such narrow gaussian component may come from the thermal radiation of cores in molecular cloud, or reproduced by low-velocity shocks (Louvet et al. 2016). And low-velocity shocks are usually attributed to colliding flows or cloud-cloud collision (Jiménez-Serra et al. 2010; Nguyen-Lu'o'ng et al. 2013; Louvet et al. 2016; Liu et al. 2020a). As shown in Fig. 10, the narrow components of SiO (2-1) emission lines at knots C, E and F (the knot chain marked by green dashed line in Fig. 9) are blueshifted with respect to the H^{13}CO^+ J=1-0 emission, al-

though these knots are located within the redshifted outflow lobe. It is contrary to the broad components which are redshifted with respect to the systemic velocity, indicating that the narrow components of SiO (2-1) emission lines at these knots may not be likely produced by outflow. The SiO J=2-1 emission at knot D has smallest line width of 2.65 km s^{-1} and is peaked at similar velocity as H^{13}CO^+ J=1-0 emission. The SiO J=2-1 emission at knot D does not show clear high-velocity wing or broad emission, and thus it is not affected by outflows. As discussed in Sec. 4.3, the SiO knots C, D, E, and F may originate from a collision scenario. However, we cannot fully confirm this scenario with present data.

As shown in Fig. 9b, the emission of SO (3(2)-2(1)) is also strong at the positions of SiO knots, indicating that SO emission is also strengthened by outflow shock. Both the SiO (2-1) emission and SO (3(2)-2(1)) emission are strongest at the position of G286c3 (marked as "3" in Fig. 8a or Fig. 3), and the bow-shaped structures from the moment 0 maps of HCO^+ (1-0) and CS (2-1) show in Fig. 7. These evidences suggest that the formation of G286c3 is possibly triggered by the outflow driven by G286c1.

4 DISCUSSION

4.1 Is G286 undergoing global collapse?

According to the model of contracting clouds (e.g. Leung & Brown 1977; Zhou et al. 1993; Myers et al. 1996), a pair of optically thick and thin lines can be used for identifying infall motions. The optically thin line should show a single-peaked profile, which helps to rule out the possibilities of other gas kinematics (e.g., rotation or multiple velocity components). In contrast, the optically thick lines of contracting clouds often show double-peaked profiles with

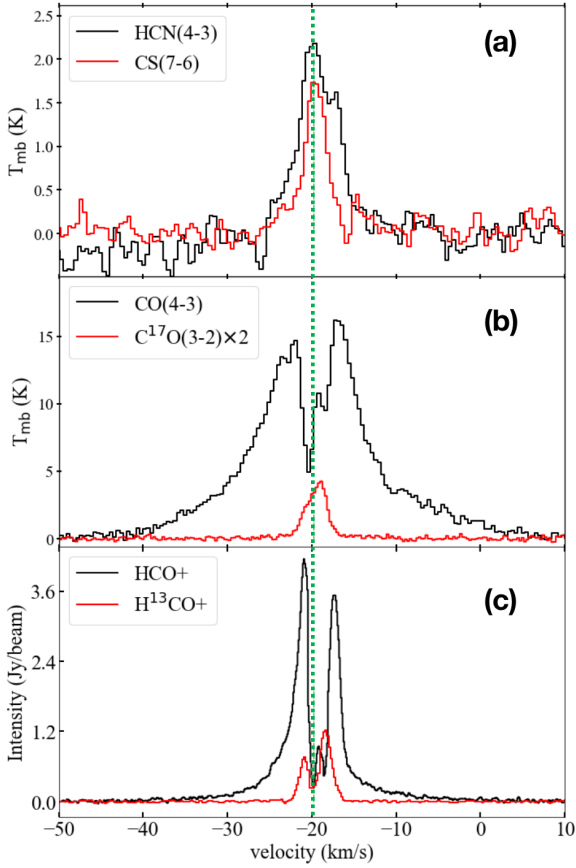


Figure 5. (a) Averaged spectrum of HCN(4-3) (black) and CS(7-6) (red) for source G286 by ASTE; (b) Averaged spectrum for source G286 by APEX, black and green curves denote the CO(4-3) and C¹⁷O(3-2) lines; (c) HCO⁺(1-0) and H¹³CO⁺(1-0) spectrum in G286 with ACA 7m array data averaged over a region with diameter 36'' (the beam size of B10). Vertical dashed green line indicates the systemic velocity at $V_{LSR} = -19.8 \text{ km s}^{-1}$.

blueshifted one stronger than the redshifted one. Such "blue profile" can be well produced by radiation transfer models for contracting clouds with density and temperature gradients (e.g. Zhou et al. 1993; Myers et al. 1996; Lee et al. 1999).

B10 argued that G286 is undergoing global collapse through analyzing the J=1-0 and J=4-3 transitions of HCO⁺ and H¹³CO⁺ lines obtained in single dish observations. However, the optically thin line H¹³CO⁺ is very weak and fuzzy in Fig.4 of B10 due to the low resolution and sensitivity in their single-dish observations. They argued that H¹³CO⁺ line is single peaked and regarded it as an important evidence to testify the existence of global infall in the G286 region. However, the results of our higher resolution ALMA array data show the profile of optically thin line H¹³CO⁺(1-0) is double-peak in Fig. B2 and Fig. 5(c). In Fig.2 of C20, they presented spectra of CO(2-1), C¹⁸O(2-1), N₂D⁺(3-2) and DCO⁺(3-2) averaged over an area with 2.5' in radius centered on the phase center. The line profile of optically thick CO is single-peaked, but the line profiles of optically thin molecules are double-peaked. So the line profiles of C20 are different from the profiles by B10 and our study. C20 also analyzed the spectral-line profiles of individual cores (Appendix B of C20), they found that both the optically thin and optically thick molecular spectral-lines of G286c3 show double-peak profiles, and they attribute this to two different velocity components. In our ALMA observations, the optically thick and

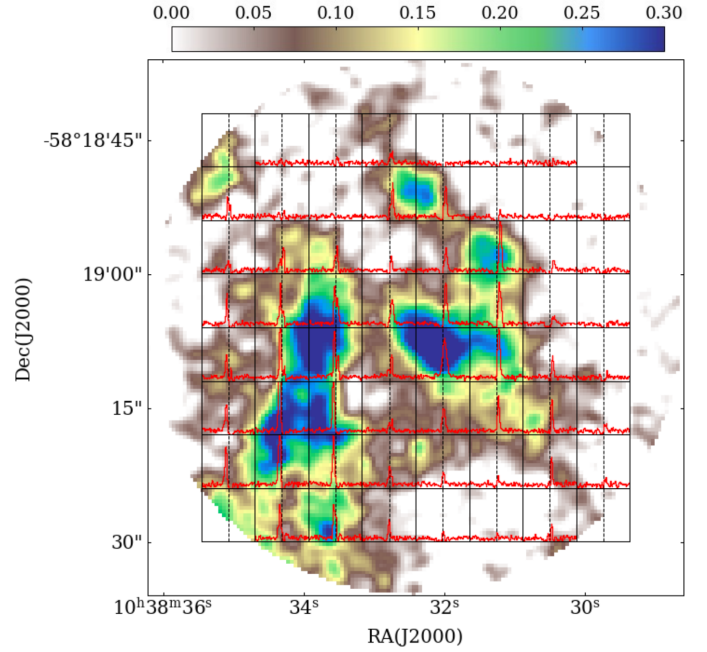


Figure 6. The grid map of H¹³CO⁺(1-0), background map is the moment 0 map of H¹³CO⁺, the side-length of each square lattice is 15 pixels. The line profile is the averaged one of the data in each square lattice, drawn in the velocity range of (-35 km s⁻¹, -5 km s⁻¹). Black dashed lines in the middle mark the systemic velocity. The color bar on the top indicates the flux scale in Jy beam⁻¹ km/s for moment 0 map.

thin lines (such as HCO⁺(1-0), H¹³CO⁺(1-0) and CCH(1-0)) also show double peaked profiles. As discussed in the previous sections, the double peaked profiles are caused by other bulk motions (e.g., relative motions of two sub-clumps, outflows) as well as global infall within the clumps.

In short, infall motion in distant massive clumps should not be the only cause of producing blue profile of molecular lines in single dish observations. Thus, we advise great caution in interpreting gas kinematics (e.g., infall) from line profiles toward distant massive clumps in single dish observations. It is simply because that the low resolution single-dish observations can not resolve the complex gas motions within distant massive clumps (Wu & Evans 2003; Fuller et al. 2005; He et al. 2015; Yue et al. 2021).

Although the "blue profile" of optically thick line emission in single dish observations of G286 (like B10) is not likely caused by gas infall motions, this cannot rule out the possibility that G286 is still undergoing overall collapse. Following Wu et al. (2010), the virial mass of the dense clump is calculated by

$$M_{Vir} = \frac{5R\Delta v^2}{8a_1a_2G\ln 2} \sim 209 \frac{(R/1pc)(\Delta v/1km/s)}{a_1a_2} M_{\odot} \quad (2)$$

$$, a_1 = \frac{1-p/3}{1-2p/5}, p < 2.5. \quad (3)$$

where a_1 is the correction for a power-law density distribution ($n(r) \propto r^{-p}$) and a_2 is the correction for a nonspherical shape (Bertoldi & McKee 1992). In Sec. 3.1, we assume the spherical geometry of clump, $a_2 = 1$. To calculate a_1 , we take the average value $p \sim 1.77$ (Mueller et al. 2002) for all massive dense clumps. The linewidth of H¹³CO⁺ J=1-0 is $\Delta v \sim 1.46 \text{ km s}^{-1}$ by fitting the ACA

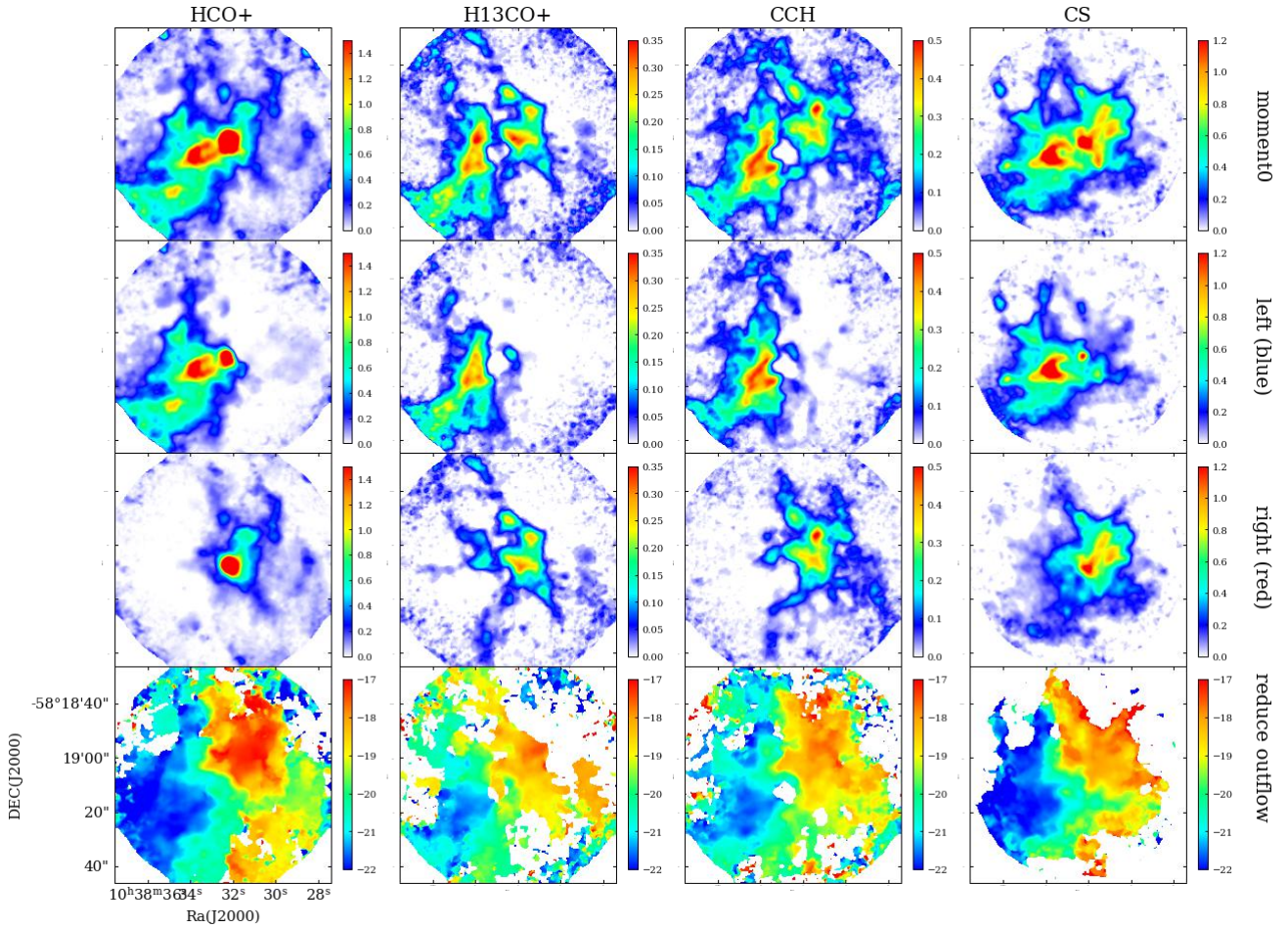


Figure 7. Rows from left to right show the moment maps of HCO⁺ (1-0), H¹³CO⁺ (1-0), CCH (1-0), and CS (2-1) with 7m+12m data. From top to bottom, the color scales show 7m+12m moment 0 maps of the whole [velocity range is (-60 km s⁻¹, 20 km s⁻¹)], 7m+12m moment 0 of the left [blueshift, velocity range is (-60 km s⁻¹, -19.8 km s⁻¹)], 7m+12m moment 0 of the right [redshift, velocity range is (-19.8 km s⁻¹, 20 km s⁻¹)], 7m+12m moment 1 maps of the whole reduced outflow. For eliminating outflow, the velocity range is limited as (-23 km s⁻¹, -16.5 km s⁻¹). The color bar on the right indicates the flux scale in Jy beam⁻¹ km/s for moment 0 maps and velocity scale in km s⁻¹ for moment 1 maps.

7m spectral line (see Fig. 5(c)) with two Gaussian profiles. The radius R derived from H¹³CO⁺ J=1-0 emission is 0.40 ± 0.05 pc (see B10). Then the virial mass of G286 clump is $M_{vir} \sim 126 M_{\odot}$, which is significantly smaller than the total mass of G286 clump. This indicates that the G286 clump is still bounded by gravity and may be undergoing overall collapse. As discussed in next section, the energetic outflow cannot push the two sub-clumps away. In addition, G286 is also confined by external pressure from nearby HII regions. Therefore, the G286 clump will likely collapse further, and the two sub-clumps will move close to each other.

4.2 Feedback of outflows

Energetic high-velocity outflows in massive protoclusters could entrain wide-angle low-velocity materials through momentum feedback (Liu et al. 2010, 2016a; Bally 2016). Below we discuss whether the energetic outflows in G286 can drive expansion of the two sub-clumps.

The mass (M_{gas}), momentum (P_{gas}) and energy (E_{gas}) of the two sub-clumps can be estimated with line emission of H¹³CO⁺ J=1-0. The mass (M_{out}), momentum (P_{out}) and energy (E_{out}) of the

outflows can be estimated from the line emission of high velocity wings in HCO⁺ J=1-0 line. We assume that the line emission of H¹³CO⁺ J=1-0 and high velocity emission of HCO⁺ J=1-0 are optically thin.

Following the approach described in Li et al. (2019), we estimated the physical parameters of the outflows and the two sub-clumps as below. We assume that the excitation temperature of H¹³CO⁺ J=1-0 and HCO⁺ J=1-0 lines are the same and constant in both low-velocity gas and high-velocity outflow gas. Therefore, the masses are:

$$M_{out} \propto \left[\frac{H_2}{HCO^+} \right] \int_{\Omega} N_{HCO^+}(\Omega) d\Omega \propto \left[\frac{H_2}{HCO^+} \right] \int_{\Omega} \int_{v'} S_v dv' d\Omega. \quad (4)$$

$$M_{gas} \propto \left[\frac{H_2}{H^{13}CO^+} \right] \int_{\Omega} \int_{v'} S_{v'} dv' d\Omega, \quad (5)$$

The expression in bracket is the abundance ratio of molecules. The momentum of outflows and G286 sub-clump are:

$$P_{out} = M_{out}^r v_{out}^r + M_{out}^b v_{out}^b, \quad (6)$$

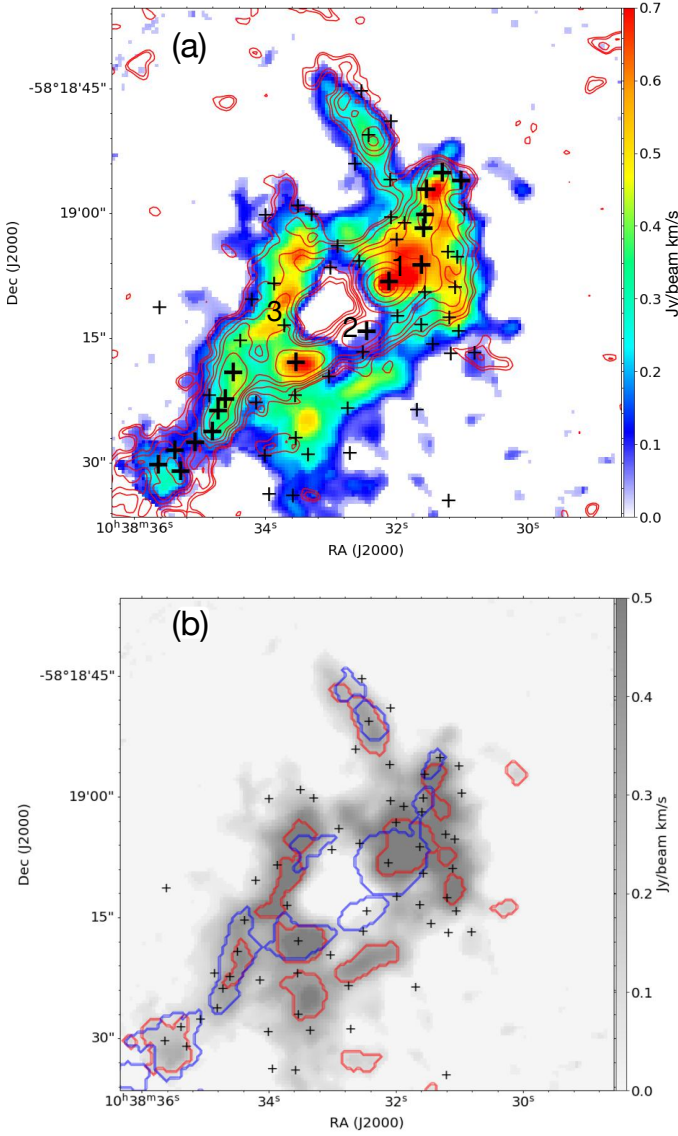


Figure 8. (a) 7m+12m moment0 map of HC_3N (11-10) in color, red contours show the 3 mm continuum image for ALMA 12+7m array data. Contour levels are $1\sigma \times (1.5, 2, 3, 4, 5, 7.5, 15, 25, 45, 60)$ with $\sigma = 0.21$ mJy/beam; (b) Blue contours are the clumps found by dendrogram algorithm with 3mm continuum. Red contours are the clumps found by dendrogram algorithm with the moment0 map of HC_3N . Cross marks "+" represent dense cores identified by C20.

$$P_{\text{gas}} = M_{\text{gas}}^r v_{\text{gas}}^r + M_{\text{gas}}^b v_{\text{gas}}^b. \quad (7)$$

From above formulas, we get the momentum ratio:

$$\frac{P_{\text{out}}}{P_{\text{gas}}} \approx \left[\frac{\text{H}^{13}\text{CO}^+}{\text{HCO}^+} \right] \frac{S_{\text{HCO}^+}^r v_{\text{out}}^r + S_{\text{HCO}^+}^b v_{\text{out}}^b}{S_{\text{H}^{13}\text{CO}^+}^r v_{\text{out}}^r + S_{\text{H}^{13}\text{CO}^+}^b v_{\text{out}}^b}. \quad (8)$$

Here v^r and v^b are the characteristic velocities of redshifted and blueshifted gas. S^r and S^b are the corresponding total flux. The total flux can be estimated from the moment 0 maps of HCO^+ and H^{13}CO^+ . The redshifted velocity v^r and blueshifted velocity v^b are defined as the median velocities of outflow lobes or sub-

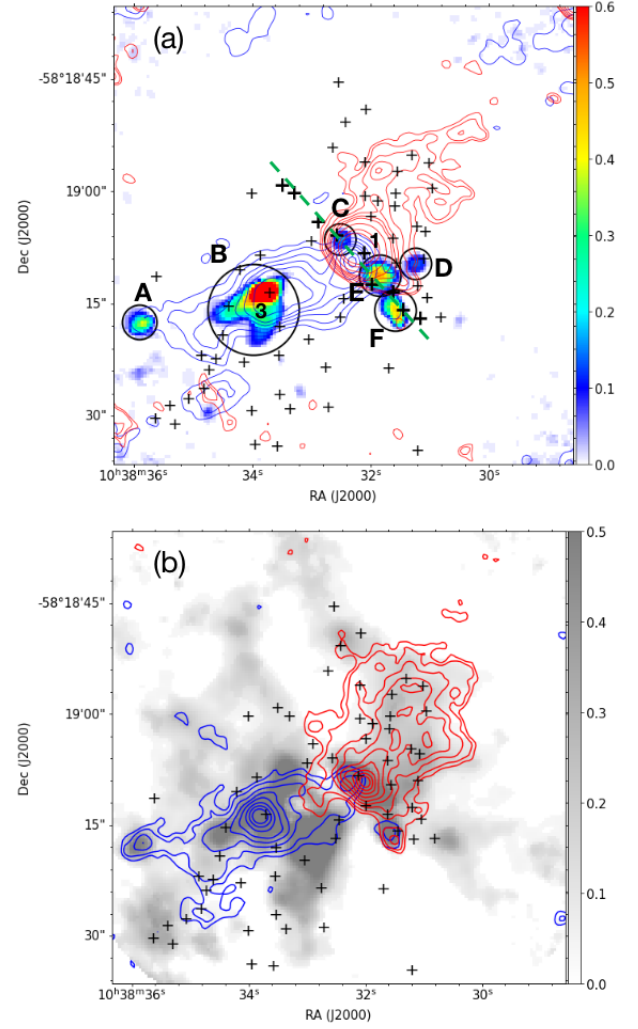


Figure 9. (a) Contour of outflow traced by HCO^+ (1-0) superimposed on the moment 0 map of SiO (2-1), color bar on the right indicates the flux scale in $\text{Jy beam}^{-1} \text{ km/s}$. SiO emission only concentrate on several positions marked as A, B, C, D, E, F. Black circles represent the range of averaged spectra at each position. The SiO knot chain and core chain are marked by green dotted line. Contour levels for blue lobe are (0.2, 0.3, 0.5, 0.7, 0.9, 1.2, 1.5, 1.8) $\text{Jy beam}^{-1} \text{ km/s}$, (0.15, 0.2 to 1.1 by steps 0.1, 1.5, 2) $\text{Jy beam}^{-1} \text{ km/s}$ for red lobe; (b) Contour of outflow traced by CS superimposed on the moment 0 map of SO . Contour levels for blue lobe are (0.15, 0.3, 0.5, 0.7, 0.9, 1.2, 1.5, 1.8) $\text{Jy beam}^{-1} \text{ km/s}$, (0.15, 0.2, 0.3, 0.4, 0.5, 0.6, 0.9, 1.5, 2) $\text{Jy beam}^{-1} \text{ km/s}$ for red lobe. The velocity intervals for redshifted and blueshifted high velocity emission of HCO^+ (1-0) and CS (2-1) lines are defined as $[-16.5, 5] \text{ km s}^{-1}$ and $[-41, -23] \text{ km s}^{-1}$, respectively.

clumps in the moment 1 maps. After subtracting the systemic velocity, the median intensity-weighted velocities of the redshifted and blueshifted outflows are $v_{\text{out}}^r \sim 3.5 \text{ km s}^{-1}$ and $v_{\text{out}}^b \sim 3.8 \text{ km s}^{-1}$, respectively. Similarly, we obtained $v_{\text{gas}}^r \sim 1.0 \text{ km s}^{-1}$ for the redshifted sub-clump and $v_{\text{gas}}^b \sim 1.1 \text{ km s}^{-1}$ for the blueshifted sub-clump. Taking $[\text{H}^{13}\text{CO}^+/\text{HCO}^+] \sim 1/60$ (Milam et al. 2005), the momentum ratio is $P_{\text{out}}/P_{\text{gas}} \sim 0.07$. Although there are many uncertainties (e.g., excitation temperature, optical depths and abundances) in above analysis, the momentum of the outflows seems much smaller than that of the two gas clumps.

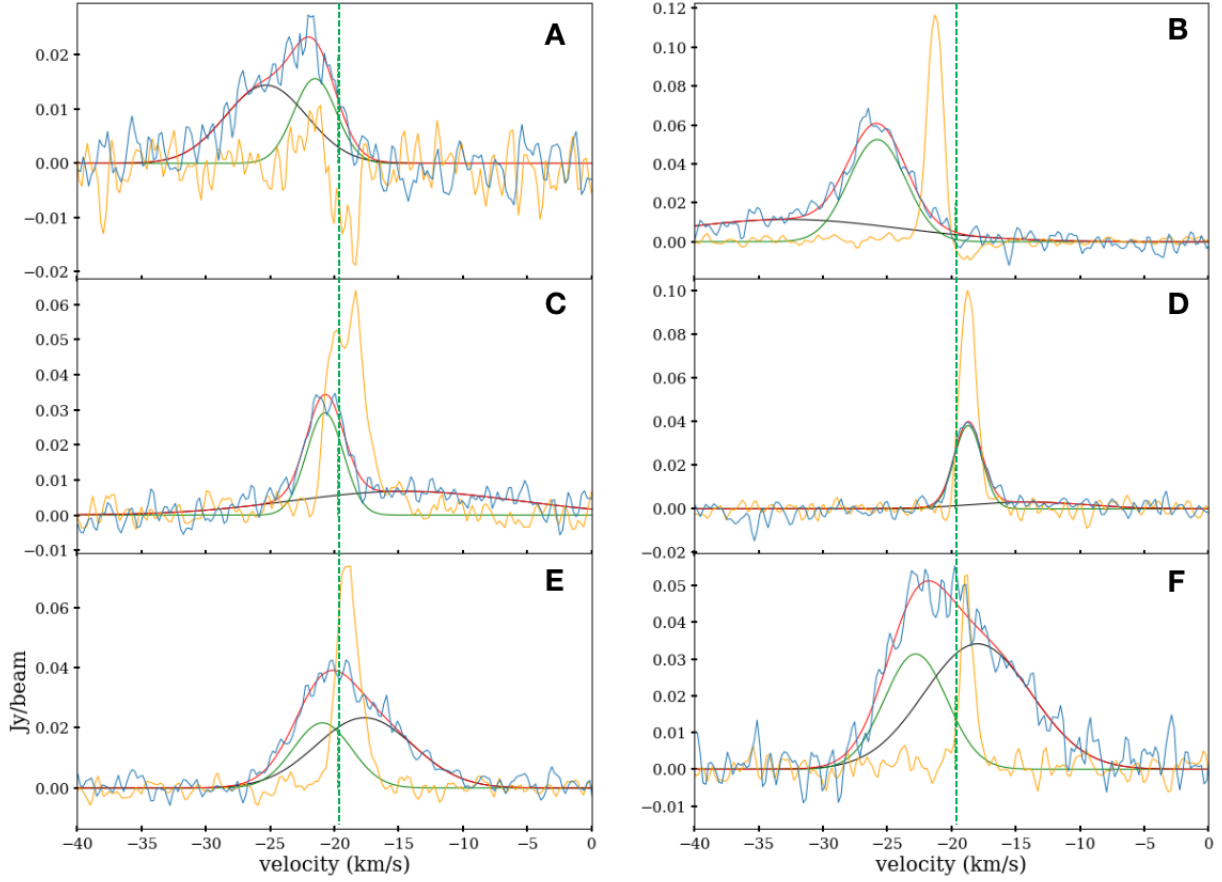


Figure 10. Averaged spectra of six positions marked by black circles in Fig. 9. The SiO (2-1) and H^{13}CO^+ (1-0) spectra are drawn in blue and orange lines, respectively. Black and green lines are to indicate the decomposed components of SiO(2-1) line and red spectral line is the result of double Gaussian fitting for SiO (2-1) line. Vertical green dotted line marks the systemic velocity.

Further we can calculate the ratio of energy:

$$E_{\text{out}} = \frac{1}{2}M_{\text{out}}^r(v_{\text{out}}^r)^2 + \frac{1}{2}M_{\text{out}}^b(v_{\text{out}}^b)^2, \quad (9)$$

$$E_{\text{gas}} = \frac{1}{2}M_{\text{gas}}^r(v_{\text{gas}}^r)^2 + \frac{1}{2}M_{\text{gas}}^b(v_{\text{gas}}^b)^2, \quad (10)$$

then we obtain $E_{\text{out}}/E_{\text{gas}} \sim 0.24$. The momentum and energy of outflows in G286 are significantly smaller than those of the two gas sub-clumps, indicating that the outflows are not capable of driving the two sub-clumps.

The dynamical time of outflow can be calculated by

$$t_{\text{dyn}} = \frac{\lambda_{\text{max}}}{(v_{\text{max}}^b + v_{\text{max}}^r)/2}. \quad (11)$$

The length of longer blue lobe (λ_{max}) is ~ 0.40 pc. v_{max}^r and v_{max}^b are the maximum velocities of redshifted and blueshifted outflow lobes, respectively. We obtain $t_{\text{dyn}} \sim 1.13 \times 10^4$ yr, which is consistent with the fact that G286 is a very young cluster. However, here we don't consider the projection effect. From above analysis, we argue that the outflow feedback in G286 is not sufficient to drive expansion of the two sub-clumps or to cause the large-scale velocity gradients across the whole G286 region. In particular, outflows cannot explain the large-scale velocity gradient along the south-west to north-east direction (see Fig. 11b). In addition, there are no outflows in the northern region close to the HII region A. Therefore,

velocity gradients in regions adjacent to HII region A (see Fig. 11c) are more likely caused by the expansion of HII region rather than outflows.

4.3 Formation of the "L" type filament and the G286 protocluster

As shown in Fig. 11(a), the HII region A seems to strongly interact with the G286 clump. The intensity gradient of $8 \mu\text{m}$ emission associated with HII region A is found to increase toward the G286 clump, suggesting that the HII region is compressing the molecular gas of G286 clump. Fig. 11(b) presents the moment 1 maps of HCO^+ J=1-0. Overall, there is a clear velocity gradient along the north-west to south-east direction. Fig. 12(a) shows the position-velocity (PV) diagram of CS J=2-1 along the black dashed arrow in Fig. 11(a). The velocity gradient inferred from this PV diagram is about $14 \text{ km s}^{-1} \text{ pc}^{-1}$. In addition, we also identified a velocity gradient along the south-west to north-east direction, which is across the "NW-SE" filament of G286. Fig. 12(b) presents the position-velocity (PV) diagram of CS J=2-1 along the red dashed arrow in Fig. 11(a), which reveals a velocity gradient of about $13 \text{ km s}^{-1} \text{ pc}^{-1}$. We also display the PV diagrams of HCO^+ J=1-0, H^{13}CO^+ J=1-0, and CCH J=1-0 for both directions mentioned above in Appendix. C, and all of those PV diagrams show distinct velocity gradients similar to that of CS J=2-1 in Fig. 12.

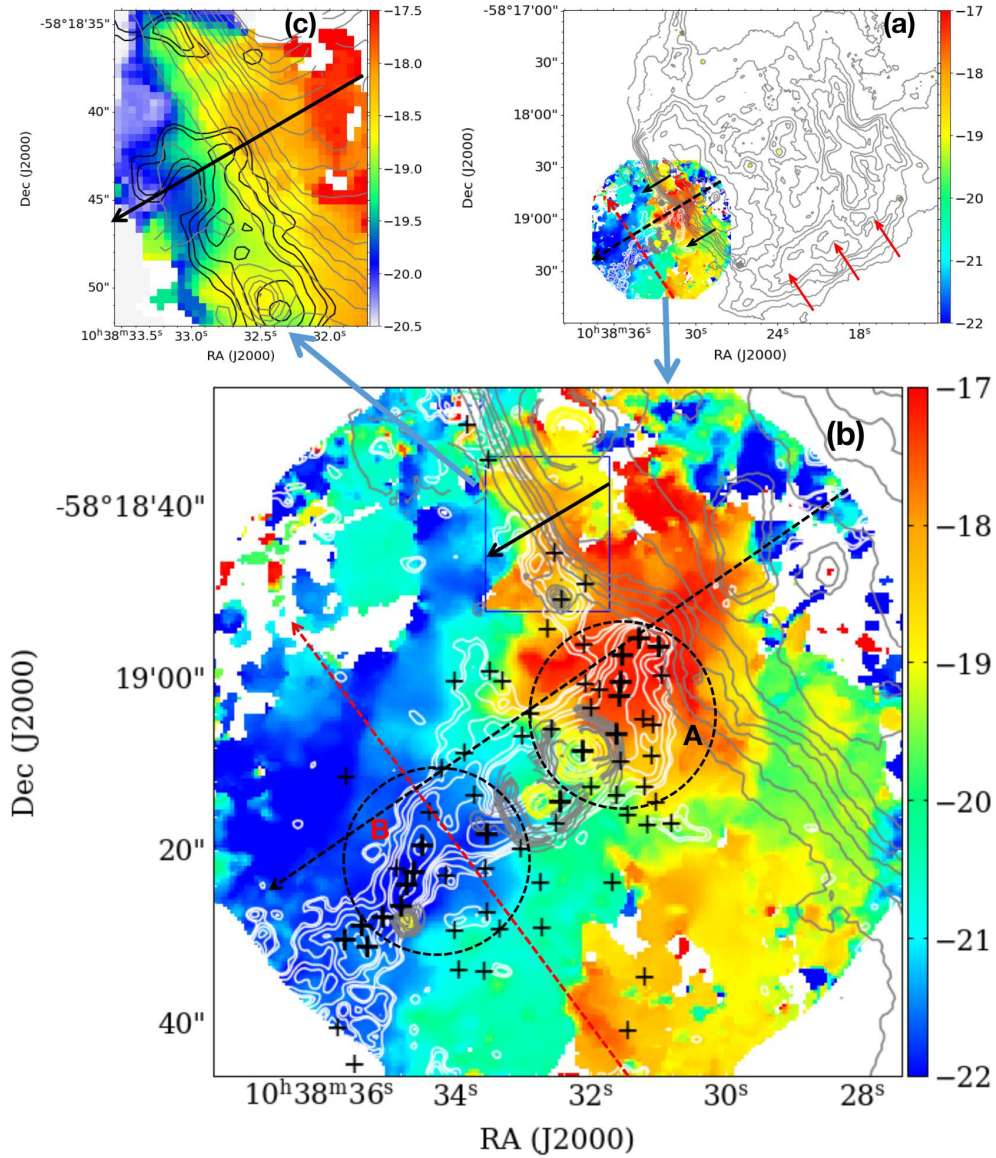


Figure 11. (a) Lower left is the velocity field in G286 region traced by HCO⁺ (1-0), here we reduce the outflow (as Fig. 7 shows). White contour represents the emission of 3 mm continuum. Grey contours (Spitzer 8 μm emission) show the HII region A. Black arrows indicate the approximate extrusion direction of HII region A, red arrows for HII region B. Dashed black arrow and red arrow indicate the velocity gradient from extrusion. Contour levels for 3mm continuum are $1\sigma \times (1.5, 2, 3, 4, 5, 8, 12, 16, 24, 32, 48, 64, 75)$ with $\sigma=0.21$ mJy/beam; (b) 7 m+12 m moment 1 map of HCO⁺ for G286 region, for eliminating outflow, velocity range is limited as (-23 km/s, -16.5 km/s), the systemic velocity is -19.8 km/s. Yellow contours (Spitzer 4.5 μm emission) show two protostars G286c1 and G286c2, others are the same as (a). Contour levels for Spitzer 4.5 μm and 8 μm are (80, 100, 120, 140, 160, 200, 280, 360, 390) mJy/sr. Dashed black circles roughly mark two sub-clumps; (c) Velocity field of CCH (1-0), the size of region is the blue box marked in (b).

Filaments with prominent velocity gradients perpendicular to their major axes have been detected in molecular clouds (Beuther et al. 2015; Chen et al. 2020). Such velocity gradients across filaments suggest that self-gravitating filaments may form from shocked flows in molecular clouds (Chen et al. 2020). The velocity gradient in the G286 clump along south-west to north-east direction could be caused by such large-scale compression flows. The HII region A seems also to be compressed by the same large-scale flow. As indicated by the red arrows in Fig. 11(a), the contours in the southern part of HII region A are much denser than the contours in the northern part, indicating that the southern part may be compressed or confined by external pressure. As shown in Fig. 1(a), both the G286 clump and the HII region A are located to the north

of a giant HII region B (Gum31) that is excited by a massive star cluster NGC3324. They seemingly locate at the loophole of HII region B. The gas blowing from HII region B seems to be acting on them. As seen in Fig.5 of Rebolledo et al. (2016), there is a clear velocity gradient due to the expansion of HII region B. Both G286 clump and HII region A are located along that large scale velocity gradient. Therefore, we suspect that the expansion of HII region B compresses its surrounding interstellar medium and induces the large-scale velocity gradient across the “NW-SE” filament within the G286 clump. More discussions on the stellar feedback of HII region B are presented in Appendix. C. However, we cannot rule out the possibility that the large-scale velocity gradient along south-

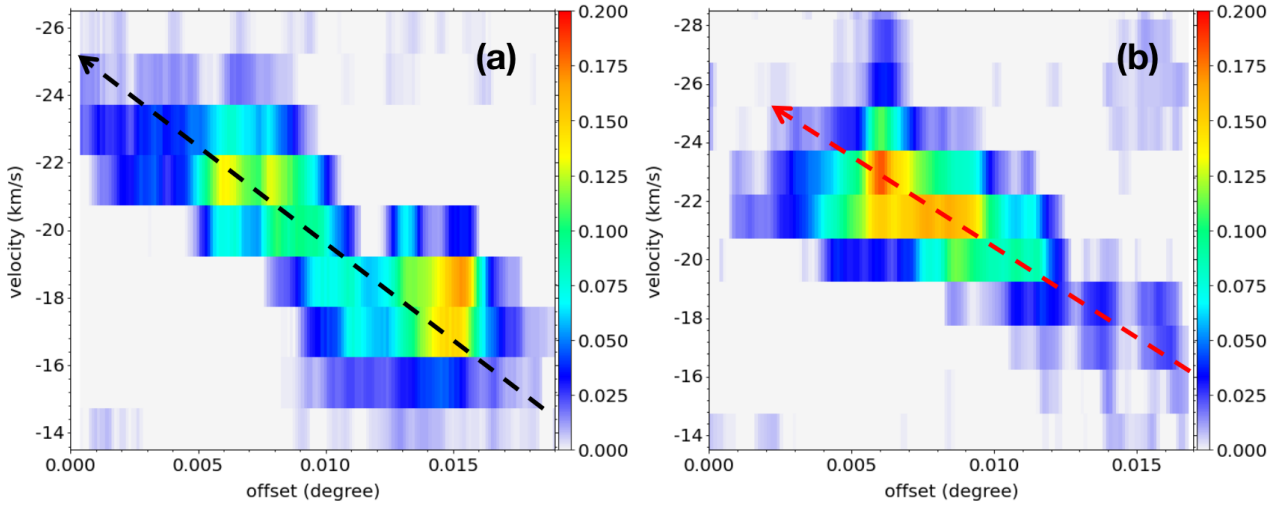


Figure 12. PV diagram of CS J=2-1 along the black and red dashed arrows in Fig. 11(a).

west to north-east direction is caused by large-scale shocked flows induced by supersonic turbulence (Chen et al. 2020).

The northern part of the G286 clump, however, is more affected by the expansion of HII region A. Fig. 11(c) shows the moment 1 map of CCH J=1-0 toward the “NE-SW” filament. CCH is a good tracer of low density PDR regions (Cuadrado et al. 2015). As shown in Fig. 11(c), there is an obvious velocity gradient across the “NE-SW” filament, which is likely caused by the expansion of the PDR of HII region A. Moreover, the 3 mm continuum emission (“NE-SW” filament) is just located in front of the PDR region, the protruding portion of 3 mm continuum emission just corresponds to the sagging portion of HII region A (right upper edge of sub-clump A in Fig. 11(b)), which also indicates that “NE-SW” filament is created by the extrusion of HII region A. At the middle region of Fig. 11(b), there is a core chain centered on G286c1 at the interface of the “NW-SE” and “NE-SW” filaments. A chain of SiO knots showing narrow line emission is also along this core chain (as shown in the green dashed line in Fig. 9(a)), which may indicate a shock front induced by the collision of the “NW-SE” and “NE-SW” filaments.

Fig. 13 presents a schematic cartoon that summarizes the key points of the formation process of the “L” type filaments and proto-clusters in the G286 clump:

(1) Two HII regions are squeezing the G286 clump. The green and cyan arrows indicate the directions of extrusion by the two HII regions and the velocity gradients induced by the compression flows.

(2) Two main filaments (“NW-SE” and “NE-SW” filaments) with prominent velocity gradients perpendicular to their major axes are formed due to the compression flows. The collision of the “NW-SE” and “NE-SW” filaments generate the “L” type structure.

(3) The filaments fragment into two subgroups of dense cores that are forming the cluster of stars. The most massive core G286c1 forms at the junction of “NE-SW” and “NW-SE” filaments. G286c1 is driving an energetic molecular outflow, which reshapes the gas distribution and creates a cavity in the “NW-SE” filament, further triggers the formation of strongly shocked core G286c3.

5 SUMMARY

We have studied the gas kinematics in G286 clump from large scale to small scale with ALMA data obtained in the “ATOMS” project. The main results are as follows:

(1) The total mass of the central region of G286 clump is estimated as $M \sim 1021 M_{\odot}$. The skeletons of sub-filaments in G286 are identified by the FILFINDER algorithm, and the most massive compact cores identified by the Dendrogram algorithm are located along the longest sub-filament with a length of ~ 0.77 pc. The width of longest filament is $W \sim 0.075$ pc. We obtain two subgroups of dense cores from a nearest neighbor separation (NNS) analysis, which are perfectly matched to the “red” group and “blue” group of C20.

(2) We demonstrate that the blue profile of molecular lines in previous studies (B10) of G286 with single dishes is actually caused by gas emission from two sub-clumps rather than gas infall. We advise great caution in interpreting gas kinematics (e.g., infall) from line profiles toward distant massive clumps in single dish observations because the low resolution single-dish observations can not resolve their complex gas motions inside.

(4) Energetic outflows are identified in G286 clump with high velocity emission in HCO^+ J=1-0 and CS J=2-1 lines. The outflow seems to be driven by G286c1 and it well aligns with the skeleton of filament. The outflow has created a cavity in G286 clump but it is not strong enough to drive expansion of the two sub-clumps.

(5) The two main filaments (“NW-SE” and “NE-SW” filaments) show prominent velocity gradients perpendicular to their major axes. The “NE-SW” filament seems to be formed due to the compression by the PDR of HII region A. We also identify a velocity gradient along the south-west to north-east direction across the “NW-SE” filament, which could be caused by the large-scale compression flows induced by the expansion of giant HII region B. The collision of the “NW-SE” and “NE-SW” filaments generate the “L” type structure in G286. And the most massive core G286c1 forms at the junction point of the “L” structure.

ACKNOWLEDGEMENTS

Tie Liu acknowledges the supports by National Natural Science Foundation of China (NSFC) through grants No.12073061 and

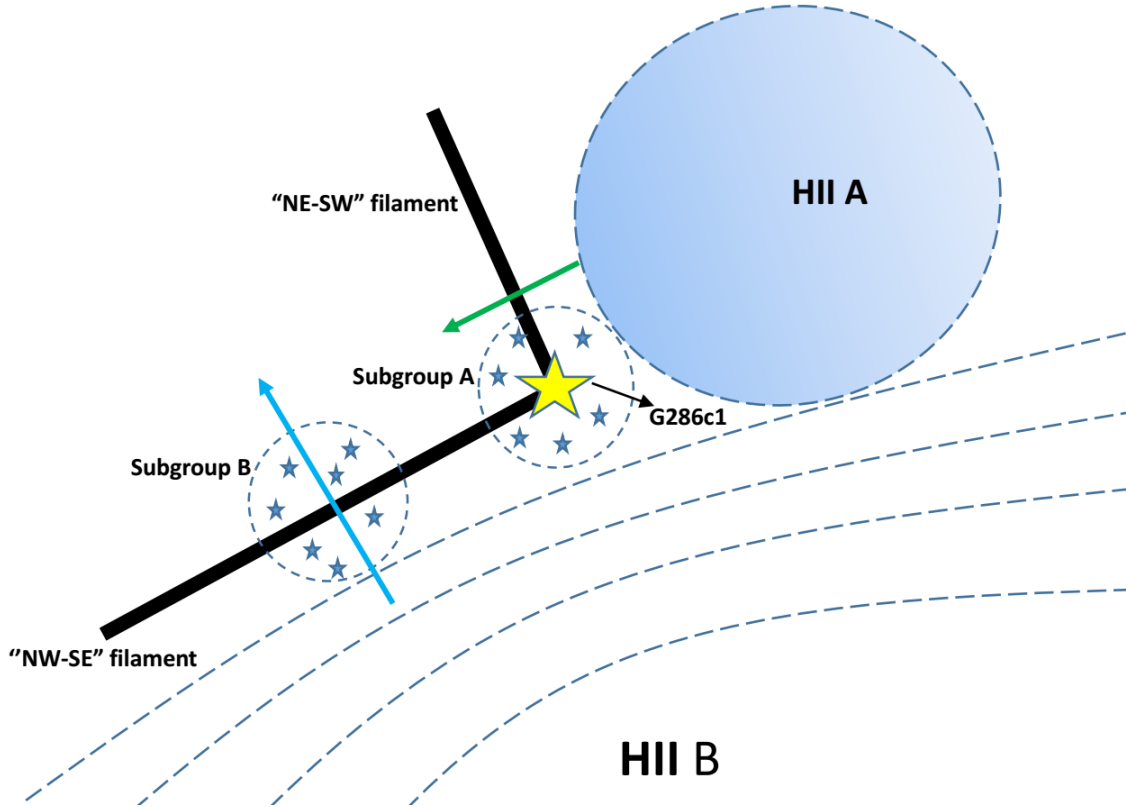


Figure 13. Schematic diagram of the star formation history in G286 region.

No.12122307, the international partnership program of Chinese academy of sciences through grant No.114231KYSB20200009, and Shanghai Pujiang Program 20PJ1415500. C.W.L. is supported by the Basic Science Research Program through the National Research Foundation of Korea (NRF) funded by the Ministry of Education, Science and Technology (NRF-2019R1A2C1010851). Guo-Yin ZHANG acknowledges the supports by China Postdoctoral Science Foundation (No. 2021T140672).

6 DATA AVAILABILITY

The data underlying this article are available in the article and in ALMA archive.

REFERENCES

- Andersen M., Barnes P. J., Tan J. C., Kainulainen J., de Marchi G., 2017, *ApJ*, **850**, 12
- André P., et al., 2010, *A&A*, **518**, L102
- André P., Di Francesco J., Ward-Thompson D., Inutsuka S. I., Pudritz R. E., Pineda J. E., 2014, in Beuther H., Klessen R. S., Dullemond C. P., Henning T., eds, *Protostars and Planets VI*. p. 27 ([arXiv:1312.6232](https://arxiv.org/abs/1312.6232)), doi:10.2458/azu_uapress_9780816531240-ch002
- Arzoumanian D., et al., 2011, *A&A*, **529**, L6
- Arzoumanian D., et al., 2019, *A&A*, **621**, A42
- Bally J., 2016, *ARA&A*, **54**, 491
- Barnes P. J., Yonekura Y., Ryder S. D., Hopkins A. M., Miyamoto Y., Fukukawa N., Fukui Y., 2010, *MNRAS*, **402**, 73
- Benjamin R. A., et al., 2003, *PASP*, **115**, 953
- Bertoldi F., McKee C. F., 1992, *ApJ*, **395**, 140
- Beuther H., Ragan S. E., Johnston K., Henning T., Hacar A., Kainulainen J. T., 2015, *A&A*, **584**, A67
- Bonnell I. A., Bate M. R., Clarke C. J., Pringle J. E., 1997, *MNRAS*, **285**, 201
- Bonnell I. A., Bate M. R., Clarke C. J., Pringle J. E., 2001, *MNRAS*, **323**, 785
- Cappa C., Niemela V. S., Amorín R., Vazquez J., 2008, *A&A*, **477**, 173
- Carey S. J., et al., 2009, *PASP*, **121**, 76
- Chen C.-Y., Mundy L. G., Ostriker E. C., Storm S., Dhabal A., 2020, *MNRAS*, **494**, 3675
- Cheng Y., Tan J. C., Liu M., Kong S., Lim W., Andersen M., Da Rio N., 2018, *ApJ*, **853**, 160
- Cheng Y., Tan J. C., Liu M., Lim W., Andersen M., 2020a, *ApJ*, **894**, 87
- Cheng Y., Andersen M., Tan J., 2020b, *ApJ*, **897**, 51
- Cosentino G., et al., 2018, *MNRAS*, **474**, 3760
- Cosentino G., et al., 2020, *MNRAS*, **499**, 1666
- Csengeri T., et al., 2016a, *A&A*, **585**, A104
- Csengeri T., et al., 2016b, *A&A*, **586**, A149
- Cuadrado S., Goicoechea J. R., Pilleri P., Cernicharo J., Fuente A., Joblin C., 2015, *A&A*, **575**, A82
- Dame T. M., Hartmann D., Thaddeus P., 2001, *ApJ*, **547**, 792
- Faúndez S., Bronfman L., Garay G., Chini R., Nyman L. Å., May J., 2004, *A&A*, **426**, 97
- Fiege J. D., Pudritz R. E., 2000, *MNRAS*, **311**, 85
- Fuller G. A., Williams S. J., Sridharan T. K., 2005, *A&A*, **442**, 949
- Gómez G. C., Vázquez-Semadeni E., Zamora-Avilés M., 2018, *MNRAS*, **480**, 2939
- Güsten R., Nyman L. Å., Schilke P., Menten K., Cesarsky C., Booth R., 2006, *A&A*, **454**, L13
- He Y.-X., et al., 2015, *MNRAS*, **450**, 1926
- Hennebelle P., André P., 2013, *A&A*, **560**, A68
- Heyminck S., Kasemann C., Güsten R., de Lange G., Graf U. U., 2006, *A&A*, **454**, L21

- Jackson J. M., et al., 2019, *ApJ*, **870**, 5
- Jiménez-Serra I., Caselli P., Tan J. C., Hernandez A. K., Fontani F., Butler M. J., van Loo S., 2010, *MNRAS*, **406**, 187
- Klein B., Philipp S. D., Krämer I., Kasemann C., Güsten R., Menten K. M., 2006, *A&A*, **454**, L29
- Koch E. W., Rosolowsky E. W., 2015, *MNRAS*, **452**, 3435
- Könyves V., et al., 2015, *A&A*, **584**, A91
- Könyves V., et al., 2020, *A&A*, **635**, A34
- Krumholz M. R., McKee C. F., Klein R. I., 2005, *Nature*, **438**, 332
- Krumholz M. R., Klein R. I., McKee C. F., 2007, *ApJ*, **656**, 959
- Lee C. W., Myers P. C., Tafalla M., 1999, in Nakamoto T., ed., *Star Formation 1999*. pp 177–178
- Leung C. M., Brown R. L., 1977, *ApJ*, **214**, L73
- Li S., Zhang Q., Pillai T., Stephens I. W., Wang J., Li F., 2019, *ApJ*, **886**, 130
- Liu H. B., Ho P. T. P., Zhang Q., 2010, *ApJ*, **725**, 2190
- Liu T., Wu Y., Wu J., Qin S.-L., Zhang H., 2013, *MNRAS*, **436**, 1335
- Liu T., et al., 2016a, *ApJ*, **824**, 31
- Liu T., et al., 2016b, *ApJ*, **829**, 59
- Liu T., et al., 2020a, *MNRAS*, **496**, 2790
- Liu T., et al., 2020b, *MNRAS*, **496**, 2821
- Louvet F., et al., 2016, *A&A*, **595**, A122
- Marsh K. A., et al., 2016, *MNRAS*, **459**, 342
- Marsh K. A., et al., 2017, *MNRAS*, **471**, 2730
- McKee C. F., Tan J. C., 2003, *ApJ*, **585**, 850
- McMullin J. P., Waters B., Schiebel D., Young W., Golap K., 2007, in Shaw R. A., Hill F., Bell D. J., eds, *Astronomical Society of the Pacific Conference Series Vol. 376, Astronomical Data Analysis Software and Systems XVI*. p. 127
- Milam S. N., Savage C., Brewster M. A., Ziurys L. M., Wyckoff S., 2005, *ApJ*, **634**, 1126
- Molinari S., et al., 2010, *A&A*, **518**, L100
- Molinari S., et al., 2016, *A&A*, **591**, A149
- Motte F., Bontemps S., Louvet F., 2018, *ARA&A*, **56**, 41
- Mueller K. E., Shirley Y. L., Evans Neal J. I., Jacobson H. R., 2002, *ApJS*, **143**, 469
- Myers P. C., Mardones D., Tafalla M., Williams J. P., Wilner D. J., 1996, *ApJ*, **465**, L133
- Nguyen-Lu'o'ng Q., et al., 2013, *ApJ*, **775**, 88
- Ohlendorf H., Preibisch T., Gaczkowski B., Ratzka T., Ngoumou J., Roccatagliata V., Grellmann R., 2013, *A&A*, **552**, A14
- Peretto N., et al., 2013, *A&A*, **555**, A112
- Poglitsch A., et al., 2010, *A&A*, **518**, L2
- Rebolledo D., et al., 2016, *MNRAS*, **456**, 2406
- Smith R. J., Longmore S., Bonnell I., 2009, *MNRAS*, **400**, 1775
- Traficante A., et al., 2011, *MNRAS*, **416**, 2932
- Vázquez-Semadeni E., 1994, *ApJ*, **423**, 681
- Vázquez-Semadeni E., Gómez G. C., Jappsen A. K., Ballesteros-Paredes J., Klessen R. S., 2009, *ApJ*, **707**, 1023
- Vázquez-Semadeni E., González-Samaniego A., Colín P., 2017, *MNRAS*, **467**, 1313
- Wu J., Evans Neal J. I., 2003, *ApJ*, **592**, L79
- Wu J., Evans Neal J. I., Shirley Y. L., Knez C., 2010, *ApJS*, **188**, 313
- Yuan J., et al., 2017, *ApJS*, **231**, 11
- Yue Y.-H., Qin S.-L., Liu T., Tang M.-Y., Wu Y., Wang K., Zhang C., 2021, *Research in Astronomy and Astrophysics*, **21**, 014
- Zhang G.-Y., André P., Men'shchikov A., Wang K., 2020, *A&A*, **642**, A76
- Zhou S., Evans Neal J. I., Koempe C., Walmsley C. M., 1993, *ApJ*, **404**, 232
- Zinnecker H., Yorke H. W., 2007, *ARA&A*, **45**, 481
- Zucker C., Chen H. H.-H., 2018, *ApJ*, **864**, 152

APPENDIX A:

A1 Width of the longest filament

We employ Radfil algorithm (Zucker & Chen 2018) to measure the deconvolved FWHM as the width of filament. Based on the mask of filament created by FILFINDER algorithm (Koch & Rosolowsky 2015), Radfil can define the spine of the filaments. Along the filament spine, we extract equidistant cuts perpendicular to the smoothed spine, the approximate distance between cuts is 3 pixels. The resulting profiles are shifted such that the center coincides with the peak intensity. When fitting the profiles, we do some background subtraction by adopting the default (bgdegree=1) which specifies the inner and outer radial distances over which to perform the background fit. Then we restrict the fitting range to avoid contamination from peak structures from the other filament.

From Fig. A1(b), we can see a good single-peak profile as a whole. According to Fig. A1(a), the main deviation comes from the vicinity of G286c1. Based on the star formation history we described in Sec. 4.3, the surrounding environment of G286c1 is very complex, which may make it difficult to accurately measure the spine of filament. After performing the background subtraction, we fit the Gaussian profile out to a distance of 0.3 pc (as Fig. A1(c) and (d) shown). The statistical uncertainty on the best-fit amplitude is 0.000034 Jy beam⁻¹, and 0.00061 pc for the best-fit mean. Following Könyves et al. (2015), the deconvolved FWHM = $\sqrt{(FWHM^2 - HPBW^2)}$, where HPBW is the half-power beamwidth, for our observations, the beamwidth of 3mm continuum is $\sim 2.20''$. Finally, we obtain the deconvolved FWHM is ~ 0.075 pc.

APPENDIX B:

B1 Moment maps in ACA 7m array data

The left and right columns of Fig. B1 present the moment 0 and moment 1 maps of HCO⁺ (1-0) and H¹³CO⁺ (1-0), respectively. We also integrated the blue-shifted emission (-60 km s⁻¹, -19.8 km s⁻¹) and red-shifted emission (-19.8 km s⁻¹, 20 km s⁻¹) separately and present the integrated intensity maps in the middle two columns of Fig. B1. From these moment maps, one can see that the G286 clump is composed by two spatially separated sub-clumps with very different velocities. The blueshifted and redshifted gas components are spatially separated. This result indicates that, the double peak profiles of molecular lines in single dish observations are actually caused by gas emission from the two different velocity components (two sub-clumps) rather than gas infall.

B2 Molecular line spectra and grid maps in 7m+12m data

To confirm the two sub-clumps, we also checked the 12m+7m combined data for HCO⁺ (1-0), H¹³CO⁺ (1-0), CCH (1-0), and CS (2-1). Fig. B2 present their spectra also averaged over an area of 36'' in size. The HCO⁺ and H¹³CO⁺ lines in combined data show very

similar line profiles to the spectra in ACA 7m observations. The line profile of CCH is similar to that of H¹³CO⁺, showing double peaked profile with the redshifted one stronger than the blueshifted one (or red profile). The average spectra of CS is single-peaked, instead of a double-peak profile. This may be due to the poor spectral resolution (~ 1.5 km s⁻¹), which is not high enough to resolve the line profile. Moreover, those features described above are more apparent in the grid maps of Fig. B3.

APPENDIX C:

C1 PV diagrams

Fig. C1 presents PV diagrams of HCO⁺ J=1-0, H¹³CO⁺ J=1-0, and CCH J=1-0 along the two directions marked by long dashed black arrow and red arrow in Fig. 11(a), and all of those PV diagrams show distinct velocity gradients similar to that of CS J=2-1 in Fig. 12.

C2 Probable interactions between G286 clump, HII region A and HII region B

In Fig. C2, the long black dashed line mark the position of density enhancement, red arrow indicates the compression direction. Along the direction of red arrows, the closer to G286 clump, column density contours become the denser. There are no other objects between HII region A and HII region B, and G286 clump. HII region A and HII region B are located in the same region and HII region B is expanding (Cappa et al. 2008; Barnes et al. 2010; Ohlendorf et al. 2013; Andersen et al. 2017). Thus the compression is likely from HII region B. From Fig.5 of Rebolledo et al. (2016), there is a clear velocity gradient due to the expansion of HII region B. Both G286 clump and HII region A are located along the large scale velocity gradient. We can clearly see the velocity gradient from the direction of HII region B in Fig. 11(b). Moreover, G286 clump has an obvious morphological deformation in Fig. C2, and the southern part of HII region A is obviously dense due to the compression shown in Fig. 11(a). In Fig. C2, two short black dashed lines mark the dense column density contours. Based on previous analysis, one side is due to the compression of HII region A and the other is likely due to HII region B. Crowded black contours inside G286 clump show the 3 mm continuum emission, two short red dashed lines indicate the two filament in Fig. 3. Surprisingly, two short red dashed lines are almost parallel to the two short black dashed lines, this strongly implies that the formation of two filaments is due to the compression from two directions described above.

HII region B is at a certain distance from HII region A and G286 clump. Therefore, we cannot fully determine the compression from HII region B. However, perhaps G286 clump keeps the right distance from HII region B that G286 clump can currently exist as a young massive star formation region, if it's very close to HII region B, the powerful energy injection of HII region B is likely to blow away the matter of G286 clump directly. All of the above speculations need to be further examined.

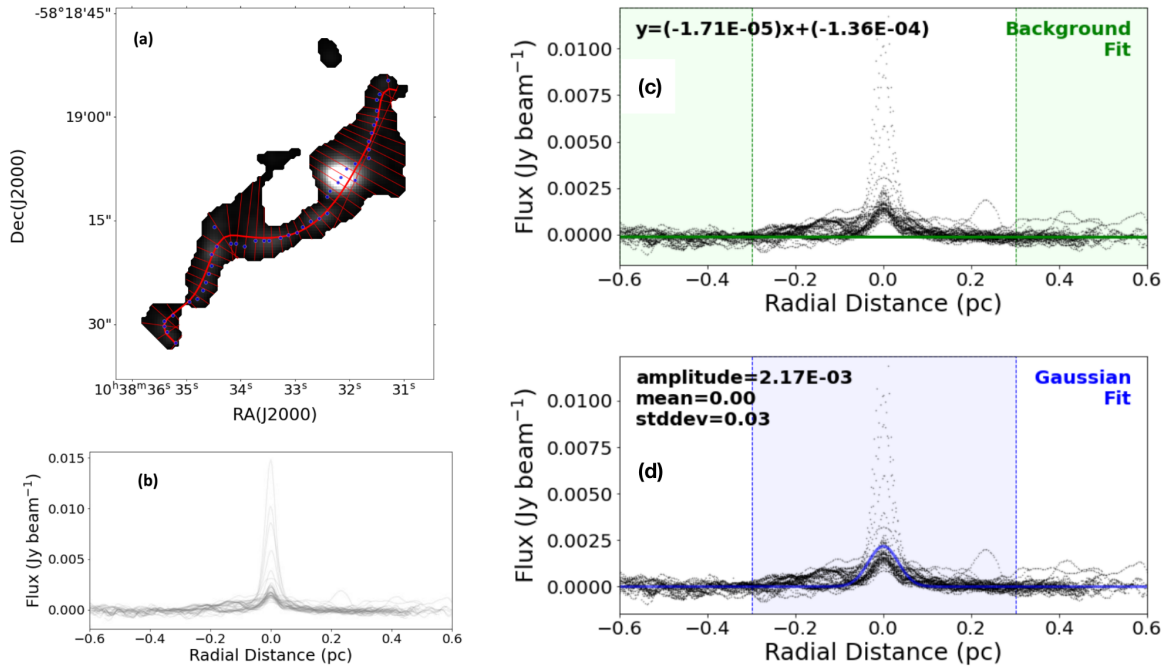


Figure A1. (a) The spines of the filaments are marked by the thick red lines in the filament mask. The perpendicular cuts are marked in thin red straight lines. The peak pixel of each intensity cut is indicated by blue dots; (b) The radial distances and density profiles of each cut; (c) The background emission, obtained by fitting over the inner and outer radial distances ($\text{bgdegree} = 1$); (d) The result of Gaussian fit, we adopt inner and outer background radii of 0.3 and 0.6 pc. After performing the background subtraction, we fit the Gaussian profile out to a distance of 0.3 pc. The range of radii over which the background and Gaussian profile are fit are highlighted in green and blue regions.

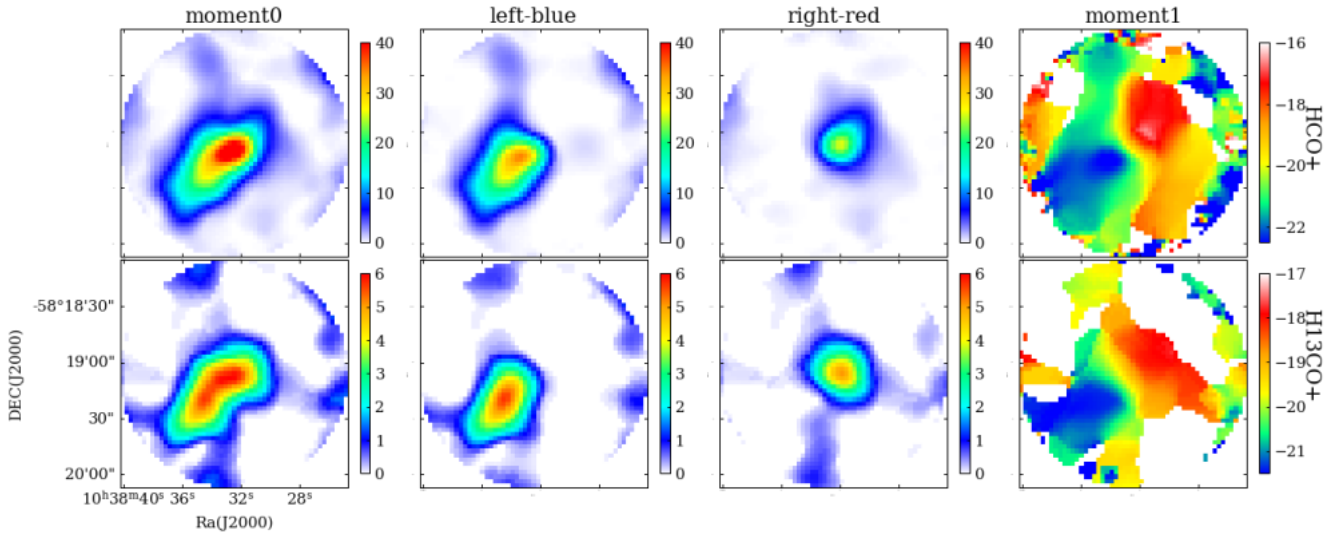


Figure B1. Columns from top to bottom show the maps of HCO⁺ (1-0) and H¹³CO⁺ (1-0) with ACA 7m array data. From left to right, the color scales show moment 0 maps of the whole [velocity range is (-60 km s⁻¹, 20 km s⁻¹)], moment 0 of the left [blueshift, velocity range is (-60 km s⁻¹, -19.8 km s⁻¹)], moment 0 of the right [redshift, velocity range is (-19.8 km s⁻¹, 20 km s⁻¹)] and moment 1 of the whole. The color bar on the right indicates the flux scale in Jy beam⁻¹ km/s for moment 0 maps and velocity scale in km s⁻¹ for moment 1 maps.

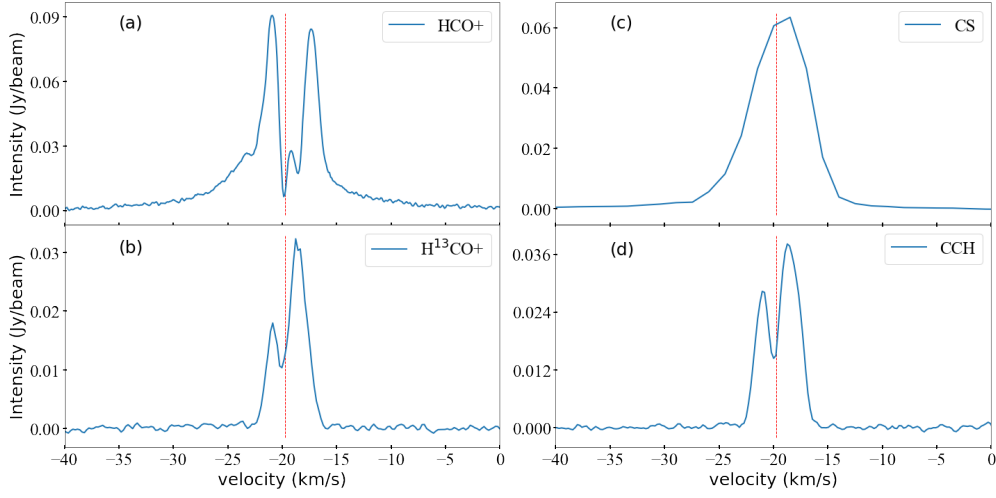


Figure B2. (a) HCO⁺ (1-0) spectrum in G286 with 7m+12m data averaged over a region with diameter 36'' (the beam size of B10), the vertical dashed red line indicates the systemic velocity at $V_{LSR} = -19.8 \text{ km s}^{-1}$; (b), (c) and (d) are the averaged spectra of H¹³CO⁺ (1-0), CS (2-1) and CCH (1-0), respectively.

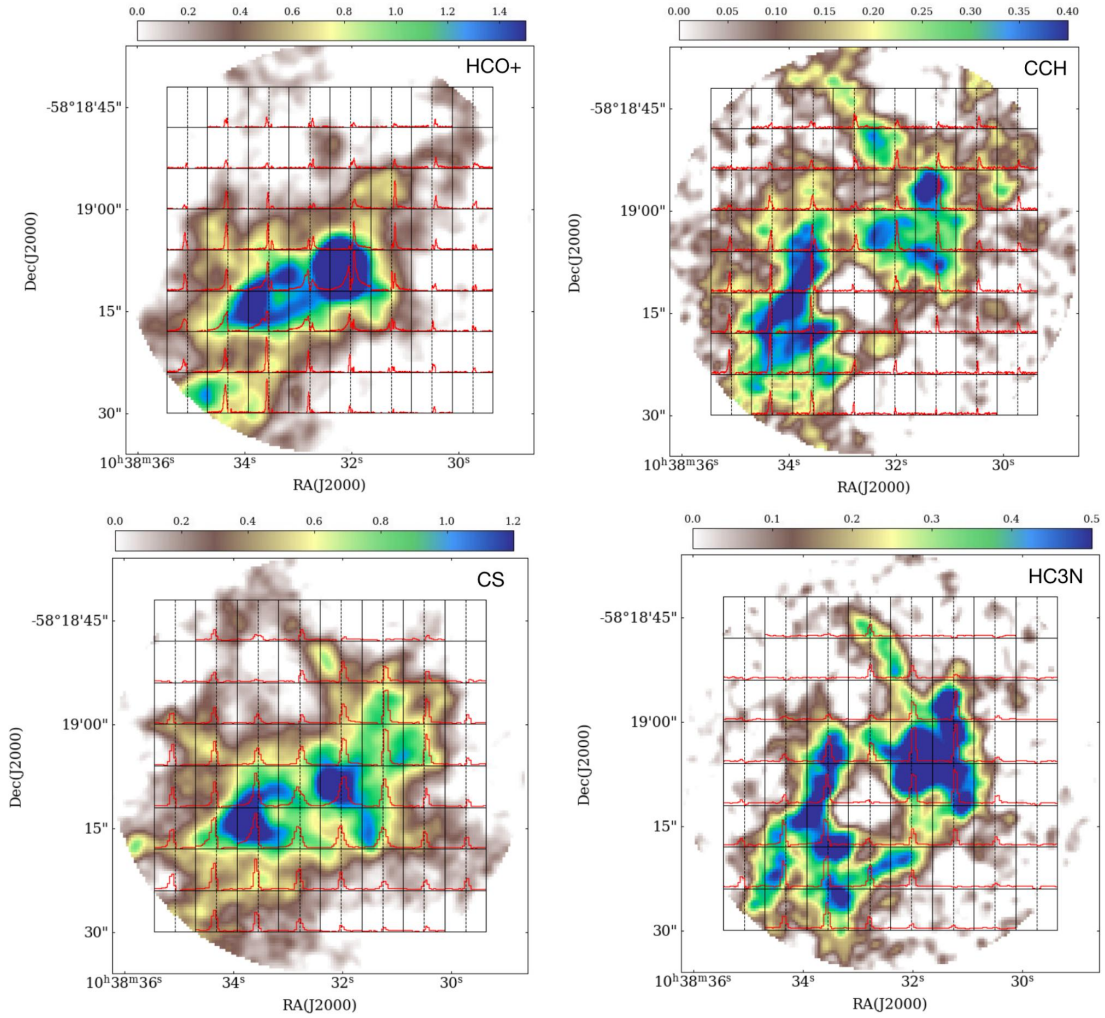


Figure B3. The grid maps of HCO⁺ (1-0), CCH (1-0), CS (2-1) and HC₃N (11-10), background map is the moment 0 maps, the side-length of each square lattice is 15 pixels. The line profile is the averaged spectra in each square lattice of each grid map, the velocity range is (-35 km s⁻¹, -5 km s⁻¹), black dashed lines in the middle mark the systemic velocity. The color bar on the top indicates the flux scale in Jy beam⁻¹ km/s for moment 0 map.

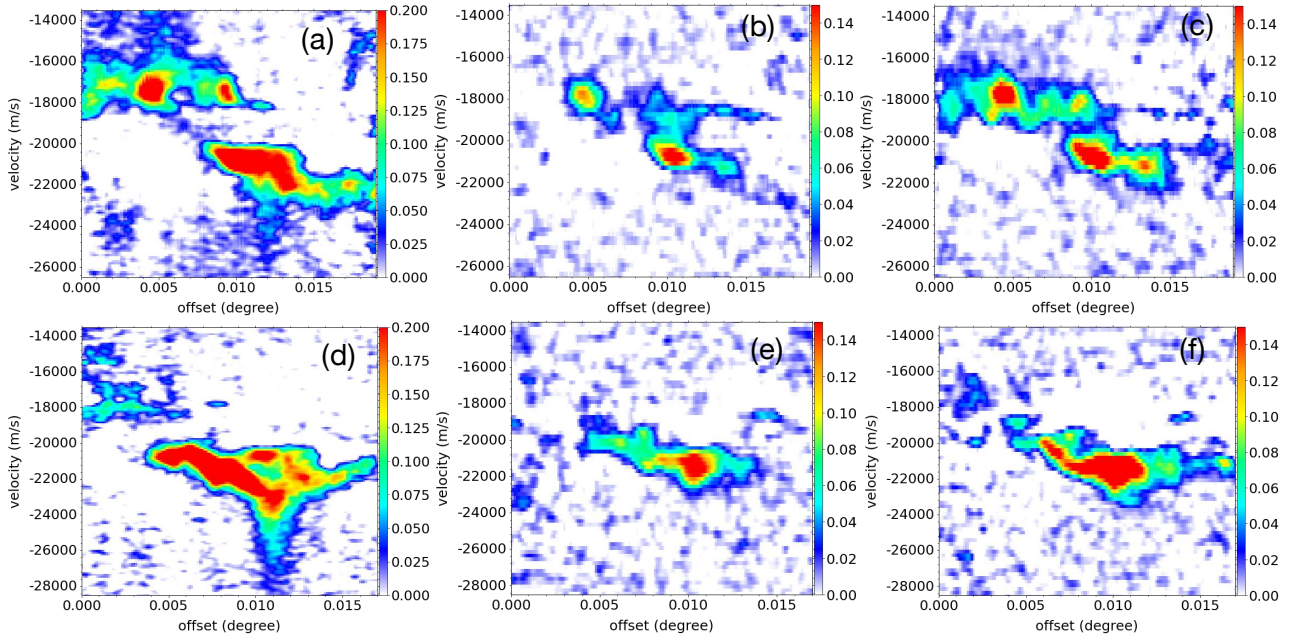


Figure C1. PV diagrams of HCO^+ $J=1-0$, H^{13}CO^+ $J=1-0$ and $\text{CCH } J=1-0$ (from left to right) along the black and red dashed arrows in Fig. 11(a). (a), (b) and (c) are along the black dashed arrow, (d), (e) and (f) for the red dashed arrow.

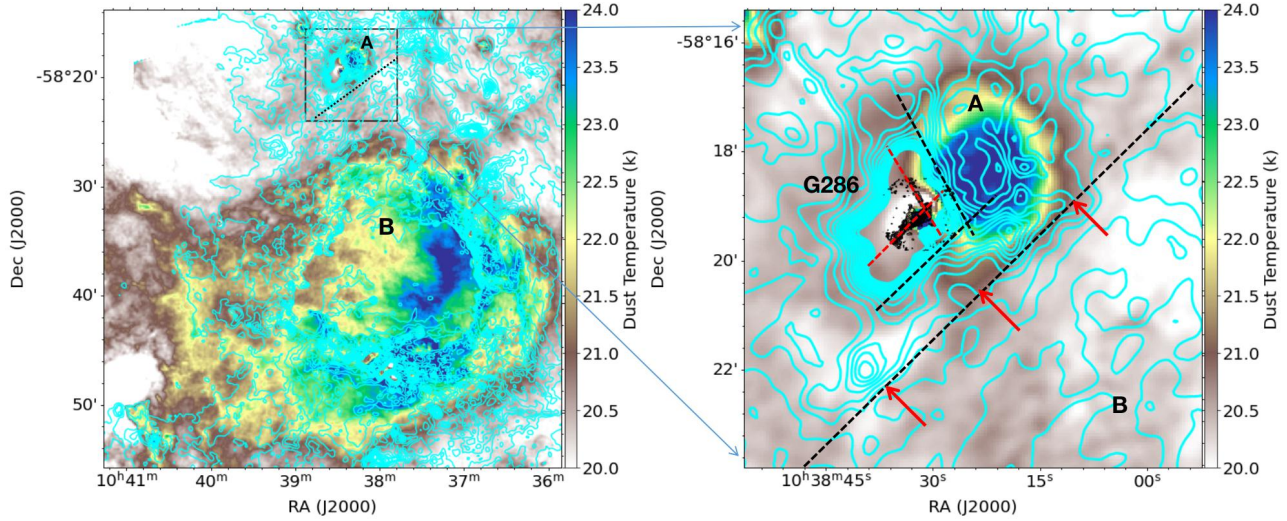


Figure C2. Background is the dust temperature map, cyan contour is the column density, all of them derive with the PPMAP procedure (Marsh et al. 2017). Column density contours are from 30 to 200, the step is 10, the unit is 10^{20}cm^{-2} . Right figure is the blow-up image in the box of left figure, crowded black contours inside G286 clump show the 3 mm continuum emission from 12m+7m data with contour levels $1\sigma \times (1.5, 2, 2.8, 3.6, 4.4$ to 12 by 0.4 steps, 12 to 15.2 by 0.8 steps, 18, 24, 30, 36, 48, 60) with $\sigma=0.21$ mJy/beam.

Author affiliations:

¹National Astronomical Observatories, Chinese Academy of Sciences, Beijing 100101, Peoples Republic of China

²University of Chinese Academy of Sciences, Beijing 100049, Peoples Republic of China

³Shanghai Astronomical Observatory, Chinese Academy of Sciences, 80 Nandan Road, Shanghai 200030, Peoples Republic of China

⁴Key Laboratory for Research in Galaxies and Cosmology, Chinese Academy of Sciences, 80 Nandan Road, Shanghai 200030, Peoples Republic of China

⁵Department of Astronomy, Yunnan University, Kunming, 650091, PR China

⁶Departamento de Astronomía, Universidad de Concepción, Av. Esteban Iturra s/n, Distrito Universitario, 160-C, Chile

⁷Kavli Institute for Astronomy and Astrophysics, Peking University, 5 Yiheyuan Road, Haidian District, Beijing 100871, People's Republic of China

⁸Department of Astronomy, Peking University, 100871, Beijing, People's Republic of China

⁹Korea Astronomy and Space Science Institute, 776 Daedeokdaero, Yuseong-gu, Daejeon 34055, Republic of Korea

¹⁰University of Science and Technology, Korea (UST), 217 Gajeong-ro, Yuseong-gu, Daejeon 34113, Republic of Korea

¹¹Physical Research Laboratory, Navrangpura, Ahmedabad—380 009, India

¹²Nobeyama Radio Observatory, National Astronomical Observatory of Japan, National Institutes of Natural Sciences, 462-2 Nobeyama, Minamimaki, Minamisaku, Nagano 384-1305, Japan

¹³IRAP, Université de Toulouse, CNRS, UPS, CNES, Toulouse, France

¹⁴Institute of Astrophysics, School of Physics and Electronic Science, Chuxiong Normal University, Chuxiong 675000, China.

This paper has been typeset from a $\text{\TeX}/\text{\LaTeX}$ file prepared by the author.